Key Points:

- Two ophiolite nappes exposed on Masirah were formed by ocean crustal accretion at 135 and 131 Ma respectively
- On-axis magmatism shows varying degrees of trace element enrichment and depletion, and is followed by Nb-enriched "near-axis" magmatism
- Similar processes may be common along modern mid-ocean ridges but masked by the homogenizing effect of an enhanced "crustal filter"

Author Contributions:

Conceptualization: C. Johan Lissenberg
Funding acquisition: Max N. Jansen, Christopher J. MacLeod, C. Johan Lissenberg
Investigation: Max N. Jansen, Daniel J. Condon
Methodology: Daniel J. Condon
Resources: Max N. Jansen, Christopher J. MacLeod, C. Johan Lissenberg
Supervision: Christopher J. MacLeod, C. Johan Lissenberg, Ian J. Parkinson
Validation: Daniel J. Condon

Relationship Between D-MORB and E-MORB Magmatism During Crustal Accretion at Mid-Ocean Ridges: Evidence From the Masirah Ophiolite (Oman)

Max N. Jansen[1] , **Christopher J. MacLeod[1]** , **C. Johan Lissenberg[1]** , **Ian J. Parkinson[2]**, and **Daniel J. Condon[3]**

[1]School of Earth and Environmental Sciences, Cardiff University, Cardiff, UK, [2]Bristol Isotope Group, School of Earth Sciences, University of Bristol, Bristol, UK, [3]NERC Isotope Geosciences Laboratory, British Geological Survey, Keyworth, UK

Abstract Enriched mid-ocean ridge basalts (E-MORB) commonly erupt at mid-ocean ridges (MOR) and seamounts, but their relationship to "depleted" MORB (D-MORB) and the processes controlling their magmatic evolution at MORs are not fully understood, hence raising more general questions about magma generation in the mantle. We here explore this conundrum through an investigation of the Masirah ophiolite (southeast Oman), a near-unique "true" MOR ophiolite. Unlike most (e.g., Tethyan) ophiolites, it was not affected by subduction and is therefore potentially able to provide valuable geological insights into the magmatic evolution of a full section of oceanic crust. Previous work has shown that the igneous crust at Masirah was thin (1.5–2.0 km) and constructed from both D- and E-MORB magmas, concluding that it formed at a slow-spreading ridge at ∼150 Ma followed by an episode of "Nb-enriched" magmatism with trace-element enrichments exceeding E-MORB during intraplate rifting ∼20 Ma later. We reinvestigate the geology of Masirah and present new field observations, geochemical data and high-precision U-Pb ages to constrain the magmatic history of seafloor spreading and off-axis magmatism. We found that D-MORB and E-MORB magmatism at Masirah was synchronous and overlapped in both composition and time with the Nb-enriched magmatism (no older than 135 Ma). Both types of magmatism were therefore integral in the formation of the Masirah ocean crust. The relationship between D-MORB and E-MORB magmatism described here may be applicable to modern MORs more broadly, but is especially prominent at Masirah due to reduced magmatism and hence a weaker crustal filter.

Plain Language Summary The oceanic crust forms approximately two-thirds of the Earth's surface and is continuously being formed at mid-ocean ridges. Due to the difficulties involved in accessing oceanic crust directly, especially the deeper stratigraphic levels, the magmatic processes involved in forming the oceanic crust remain poorly understood. Ophiolites, fragments of oceanic lithosphere that were emplaced onto the continent, can offer valuable insights to geologists, but since most ophiolites are thought to have originated in marginal oceanic basins or at the initiation of subduction, a direct comparison remains problematic. In this study, we circumvent this problem by investigating the Masirah Ophiolite, a rare example of a "true" mid-ocean ridge ophiolite. By combining field observations, geochemistry and geochronology at a level of detail not possible for present-day oceanic crust, we reconstruct the magmatic evolution of the Masirah paleoridge. We present a more accurate formation age for Masirah and find that magmatism was compositionally variable throughout crustal accretion, with later off-axis melts becoming more enriched in incompatible trace elements. We propose that the large geochemical variations observed at Masirah may be commonplace at modern mid-ocean ridges, but that these are often masked due to the typically higher volumes of magmatism that enhance mixing and homogenization.

1. Introduction

Mid-ocean ridge basalts (MORB) encompass a range of incompatible trace element compositions that is conventionally described by a global average "normal" MORB (N-MORB) composition that sits between a "depleted" (D-MORB; $La_N/Sm_N < 0.8$, normalized to primitive mantle) and an "enriched" (E-MORB; $La_N/Sm_N > 1.5$) endmember (definitions from Gale et al. (2013)). Radiogenic isotope systematics indicate these variations are related to differences in mantle source, where the enriched component is thought to be derived from pyroxenitic recycled crust (e.g., Niu et al., 1999; Prinzhofer et al., 1989; Waters et al., 2011; Yang et al., 2020)

Visualization: Max N. Jansen
Writing – original draft: Max N. Jansen
Writing – review & editing: Christopher
J. MacLeod, C. Johan Lissenberg, Ian
J. Parkinson, Daniel J. Condon

and/or metasomatized peridotite mantle (e.g., Donnelly et al., 2004; Niu et al., 2002). The recovery of E-MORB at ridge segments far from plume-fed hotspots demonstrates that the upper mantle sampled by mid-ocean ridge (MOR) magmatism is inherently heterogeneous, but its relationship to D-MORB remains poorly constrained. Side-by-side occurrences of E-MORB and D-MORB lava have been variably interpreted as temporal variations in parental melt compositions (e.g., Batiza & Niu, 1992), the existence of discrete magma plumbing systems for contemporaneously produced D- and E-MORB magmas (e.g., Perfit et al., 1994), and temporal variations in magma volumes that affect the efficiency with which contemporaneous D- and E-MORB magmas are homogenized (e.g., Waters et al., 2011).

Studies focusing on the processes that control the magmatic evolution at MORs are often limited to the sampling of lava exposed at the seafloor because of the difficulties involved in accessing deeper stratigraphic levels of oceanic crust. Ophiolites, fragments of oceanic lithosphere emplaced on the continent, are useful because they permit the study of oceanic lithosphere in three dimensions. Their use as MOR-analogs has been debated extensively, however, because the vast majority formed in atypical tectonic settings (e.g., by supra-subduction zone seafloor spreading in marginal basins or nascent "pre-arc" settings), resulting in magmas that are geochemically distinct from MORB (e.g., De Graaff et al., 2019; Goodenough et al., 2014; MacLeod et al., 2013; Miyashiro, 1973; Pearce et al., 1984).

A notable exception to the "supra-subduction" suite of ophiolites is the Masirah ophiolite, exposed on the island of Masirah, off the south-eastern coast of Oman (Peters, 2000), and distinct in age and tectonic setting from the more well-known Semail ophiolite of northern Oman. This rare "true" MOR-ophiolite is believed to represent a fragment of slow-spread ocean crust from the early Indian Ocean and preserves MORB with variable degrees of enrichment as well as an episode of off-axis magmatism (Immenhauser, 1996; Marquer et al., 1998; Meyer et al., 1996; Peters & Mercolli, 1997, 1998). Masirah therefore presents a unique opportunity to investigate the plumbing of D- and E-MORB magmas during crustal accretion as well as later off-axis magmatism.

In this study, we present new field observations and geochemical and geochronological data for Masirah to reconstruct its magmatic history, showing that the melting column underneath the ancient spreading ridge formed both D- and E-MORB magmas during the same crustal accretion episode. Additionally, we show that the MORB magmatism and off-axis magmatism partially overlap in composition and time, advancing the idea that, rather than two separate events, Masirah records the transition of on-axis seafloor-spreading to "near-axis" magmatism involving trace element enriched melts.

2. Geological Setting and Previous Work on Masirah

2.1. Masirah and the Eastern Oman Ophiolites

Masirah Island forms the largest outcrop ($\sim$650 km^2 areal extent) of the Eastern Oman Ophiolites, a series of ophiolite exposures in the Batain coastal area that also includes Ra's Madrakah ($\sim$10 km^2), several small hills near Ra's Jibsch ($\sim$1–2 km^2) and dismembered fragments in the Batain region (ranging hundreds of m^2 to several km^2; Figure 1; Immenhauser et al., 2000; Shackleton & Ries, 1990; Shackleton et al., 1990). These ophiolites are unrelated to the Tethyan Semail ophiolite and instead formed much earlier as part of the young Indian Ocean (Abbotts, 1979; Peters & Mercolli, 1998). They are thrusted over the Batain group, a series of heavily deformed allochthonous Lower Permian to Upper Maastrichtian sediments and volcanics (Gnos et al., 1997; Immenhauser et al., 1998). Although no metamorphic sole is exposed or likely to be present, stratigraphic constraints indicate that the ophiolites and Batain group were emplaced onto the continental margin sometime between the late Maastrichtian and early Paleocene, where they form a thin-skinned NW-directed fold-thrust belt covering the autochthonous rock units of the Huqf uplift and the Masirah Graben, a Mesozoic sedimentary basin (Figure 1c; Beauchamp et al., 1995; Immenhauser et al., 2000; Schreurs & Immenhauser, 1999). Extensional tectonics in the Miocene, contemporaneous with the opening of the Gulf of Aden, reactivated pre-existing faults and formed a horst-graben structure that exposes the ophiolites today (Immenhauser et al., 2000).

Emplacement of the Eastern Oman Ophiolites likely occurred during sinistral transpressive strike-slip plate motions (Barton et al., 1990; Peters, 2000; Rodriguez et al., 2016, 2020). A seismic profile through the Batain coastal area shows the heavily deformed Batain group and has been interpreted as a doubly vergent thrust stack of numerous ophiolite sheets, forming a positive flower structure (Figure 1c; Beauchamp et al., 1995; Rodriguez et al., 2020). The deep seismic structure of the south-eastern Oman continental margin reveals a highly variable
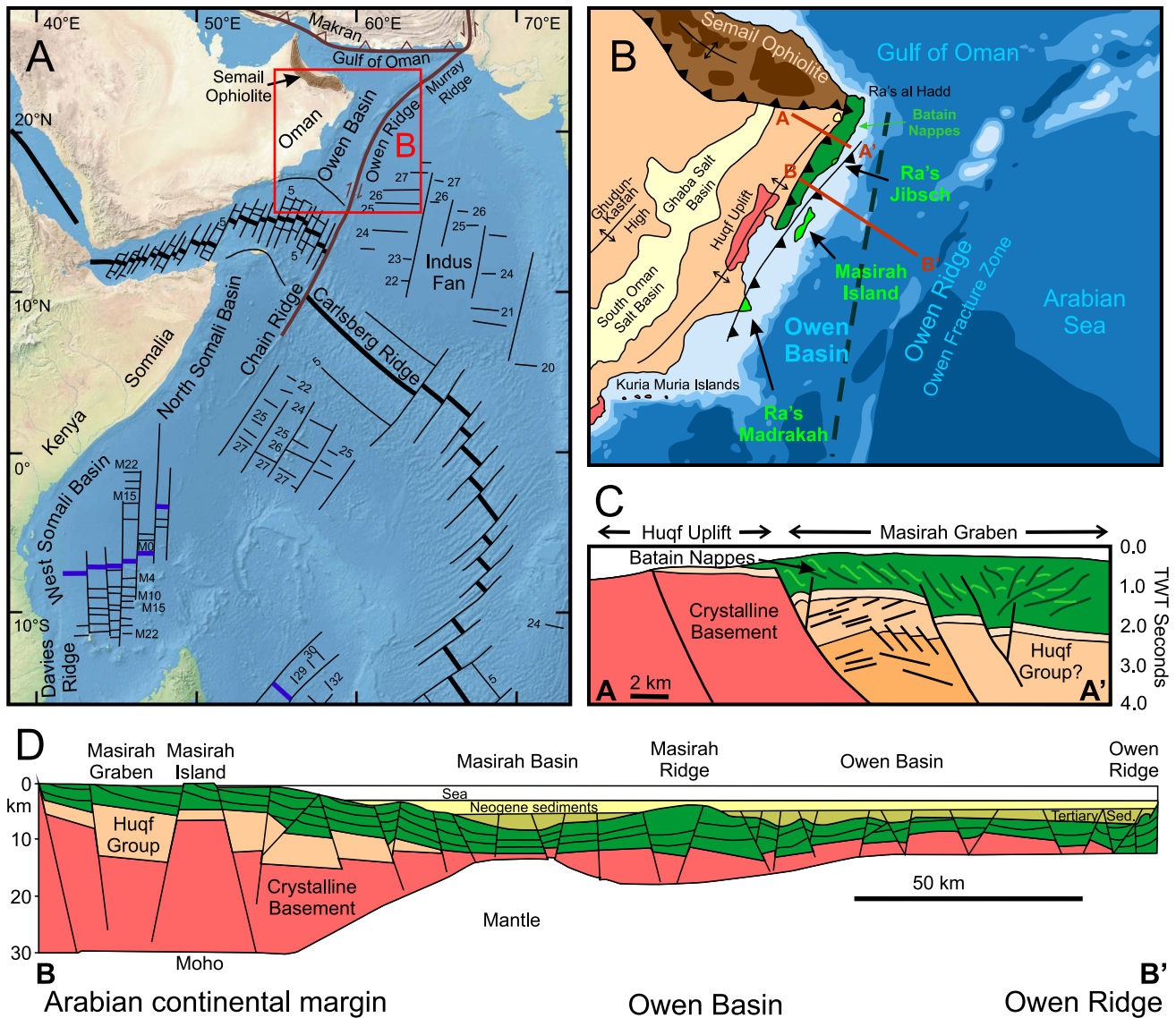
Figure 1. (a) Map of the northwestern Indian Ocean basin (after Gnos et al. (1997)) showing the location of Oman with respect to the modern Indian Ocean and Somali Basins. Thick black lines represent active spreading ridges, thick brown lines indicate transform and convergent plate boundaries, thick blue lines indicate extinct spreading ridges and magnetic anomalies are shown as labeled thin black lines (M22-M0 are magnetic anomalies between 152 and 118 Ma, while 34-21 indicate anomalies between 84 and 50 Ma). (b) Map of the Owen Basin showing the Eastern Oman Ophiolites (including Masirah), Batain Nappes and Semail Ophiolite (after Beauchamp et al. (1995) and Immenhauser et al. (2000); bathymetry from Whitmarsh (1979)). Dashed dark-blue line represents a proposed abandoned transform plate-boundary dissecting the Owen Basin (Rodriguez et al., 2016, 2020; Royer et al., 2002). (c) Simplified interpretation of a seismic cross-section across the Masirah Graben (location in b), showing a double vergent structure within the Batain Nappes that are thrust over the Masirah Graben and crystalline basement (modified from Beauchamp et al. (1995) and Rodriguez et al. (2020)). (d) Interpretation of the deep structure of the Owen Basin based on a wide-angle seismic cross-section (location in b) showing the varying depth of the Moho (after Barton et al. (1990) and Peters (2000)). The ophiolite nappes (green) extend into the Owen Basin up to the Owen Ridge, as proposed by Peters (2000).

thickness of the crystalline crust and a rough seafloor marked by several ridges, inconsistent with emplacement through simple overthrusting and instead suggestive of a strike-slip tectonic regime (Figure 1d; Barton et al., 1990). The seafloor ridges are most prominent closest to the continental margin and have been interpreted as en-échelon structures of an abandoned transform plate-boundary, analogous to modern transform ridges (Rodriguez et al., 2016, 2020). Strike-slip plate motion during emplacement is also consistent with occurrences of Cretaceous strike-slip features on the Oman mainland (Rodriguez et al., 2016).

Seismic profiles indicate a continuity between the Eastern Oman Ophiolites and the oceanic crust in the Owen Basin, which lies immediately offshore south-east from Oman, implying a common history (Figures 1c and 1d;

Barton et al., 1990; Beauchamp et al., 1995; Mountain & Prell, 1990; Rodriguez et al., 2020). Peters (2000) suggested that the Owen Basin seafloor between the Arabian continental margin and the Owen Ridge consists entirely of a series of ophiolite nappes (Figure 1d). Sedimentary constraints suggest that the eastern Owen Basin seafloor is considerably younger (Late Cretaceous; Mountain & Prell, 1990) than the ophiolites, and some authors propose that an abandoned transform plate-boundary dissects the Owen Basin, with the ophiolite sheets occurring exclusively west of this boundary (Rodriguez et al., 2016, 2020; Royer et al., 2002). A paleomagnetic study on Masirah determined a paleolatitude of 48°S ± 10° at its origin, placing it south of the Arabian continental margin and near the present-day Somali basins (Gnos & Perrin, 1996; note this is the updated figure including a calculation correction made by Peters (2000)). In their plate reconstruction, Masirah formed as part of the Indian plate during the opening of the Indian Ocean, was subsequently transported northwards when the Indian Plate changed direction, and was ultimately emplaced on the Arabian continent across a transform fault (Gnos et al., 1997; Peters, 2000; Peters & Mercolli, 1998).

2.2. Geology of Masirah

Masirah preserves a full ophiolitic suite, including mantle peridotites, lower crustal gabbros (sensu lato), upper crustal dykes and lava with D- to E-MORB compositions, and a pre-obduction sedimentary cover (Peters, 2000; Peters & Mercolli, 1998). This oceanic crustal sequence is discordantly overlain by post-obduction Paleogene limestones. Detailed mapping identified two separate ophiolite nappes and an island-wide recurring sub-horizontal thrust contact ("Main Masirah Thrust," MMT) between the deformed sedimentary cover of the Lower Nappe and the overlying mantle harzburgites of the Upper Nappe (Figure 2; Masirah North and Masirah South, 1:50,000, Peters et al., 1995). Interference between the low-angle MMT and Tertiary (i.e., post-emplacement) normal faulting is thought to have resulted in complex juxtapositions of the Upper and Lower Nappes, especially along the western coast of the island (Marquer et al., 1995, 1998). Despite this complexity and the lack of uninterrupted sections through the original ocean lithosphere, the internal structure of the nappes themselves is relatively coherent, preserving near-vertical sheeted dykes, layered gabbros sub-parallel to the crust-mantle boundary, and a gradual transition between the upper and lower crust. Marquer et al. (1998) established that the composite thickness of the original igneous oceanic crust was as little as 1.5–2.0 km, of which the gabbroic lower crust makes up <500 m, the dyke complex ∼1 km and the lava 250–500 m.

The Lower Nappe exposures, mainly situated in the south and south-east (Figure 2), resemble a classically layered oceanic crust: a lower crust of layered olivine gabbro intruded by dunitic bodies, succeeded by foliated gabbro that gradually grades upwards into a sheeted dyke complex (proportion of dolerite dykes increases from 0% to 100% up-section), which in turn is overlain by volcanics and deep-marine sediments (Peters & Mercolli, 1998; Peters et al., 1995). The sedimentary cover is subdivided into three chrono-stratigraphic units: the Maghilah Unit, the Kalban Unit, and the Fayah Unit (Immenhauser, 1996). Lava and the overlying deep-marine radiolarian-bearing Maghilah Unit of the Lower Nappe are also exposed in parts of the northern part of the island. No lower-crust/mantle boundary is exposed in the Lower Nappe and mantle exposures in the southern half of the island frequently occur as tectonically dismembered outcrops that are often associated with shallow-marine to hemi-pelagic carbonates and pelagic cherts of the Kalban Unit. The Upper Nappe exposures, in the north and north-west of Masirah, consist of more extensive mantle sections in addition to a well-exposed crust-mantle boundary and lower crust. The sheeted dyke complex is less prominent in the north but is better developed in the central part of the island. Lava associated with the Upper Nappe are rare, and no sedimentary cover is preserved.

Masirah also records the emplacement of an off-axis volcanic and plutonic suite in the Lower and Upper Nappe, respectively. The Lower Nappe contains pillow breccias interbedded with sediments of the Maghilah Unit as well as remnants of kilometer-sized, isolated submarine seamount volcanoes (notably near Shi'inzi, Figure 2; Meyer et al., 1996). These volcanics are noted for their ocean island basalt-like (OIB) light rare earth element (LREE) enrichments and have isotopic compositions that indicate a mantle source distinct from that of the lava of the main ophiolite suite (Mahoney et al., 1998). In the Upper Nappe, the off-axis magmatism is characterized by a gabbro-dolerite-granite suite of meter to kilometer-sized bodies that intrudes the pre-existing lithosphere, mainly in the mantle and at the crust-mantle boundary level, and that is absent in the Lower Nappe. The gabbros are isotropic-pegmatoids with a distinct hornblende-bearing mineral assemblage and the granites are "true" K-feldspar bearing granites that notably have Pb and Nd isotopes consistent with an oceanic mantle rather than a continental origin (Abbotts, 1978; Nägler & Frei, 1997). Additionally, late dolerite dykes that crosscut the crust in both nappes and
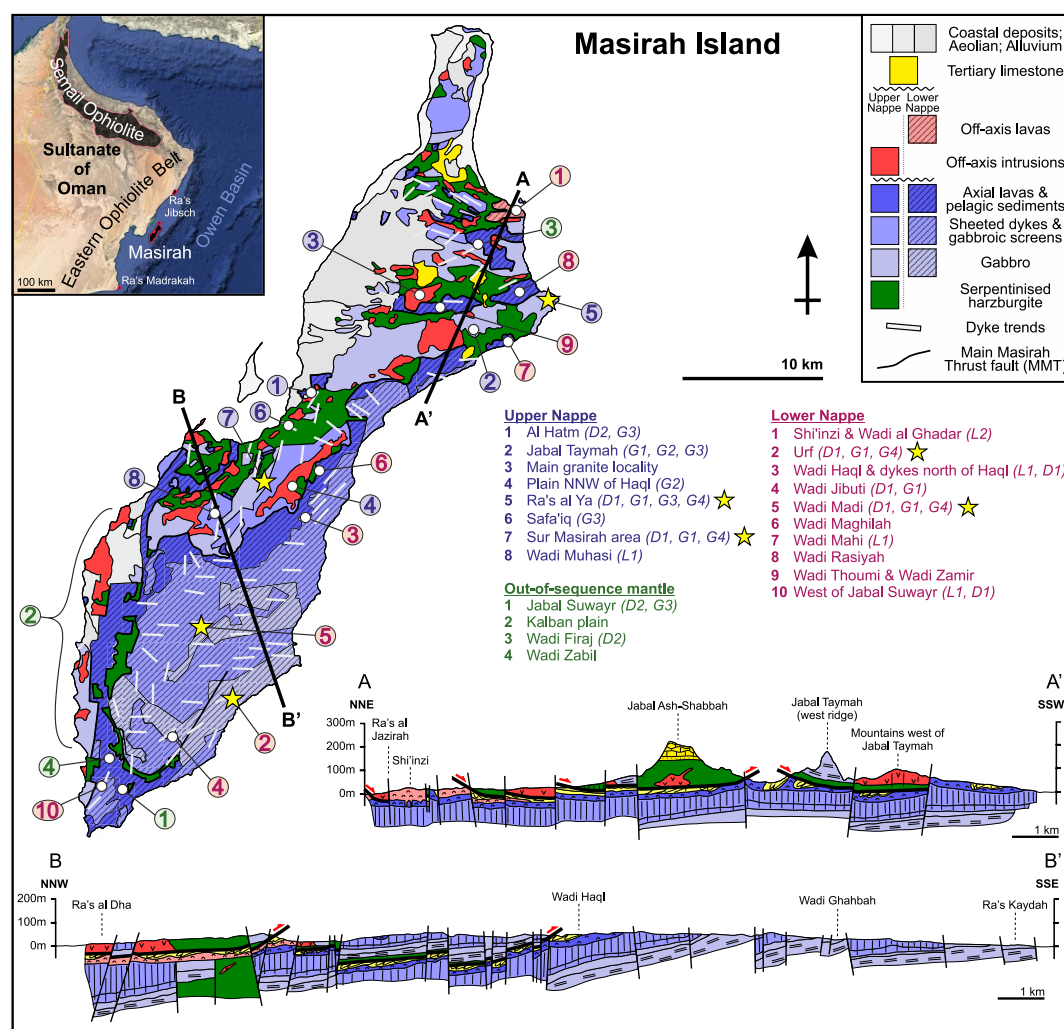
Figure 2. Geological map of Masirah with structural cross-sections through the north and south of the island illustrating the relationship between the Upper and Lower Nappes (adapted from Peters et al. (1995)). Sample locations are indicated and L1, L2, D1 etc. refer to the various lava (L), dyke (D) and gabbro (G) units studied at each location (see Figure 3 and text for more information). Geochronology sample locations are marked with a yellow star.

some mantle sections are intruded by varying proportions of gabbro and/or swarms of locally parallel dolerite dykes. Minor ductile deformation in the plutonic suite records syn- and post-emplacement extension within the plutons, and brittle extension is indicated by the late crosscutting dykes (Marquer et al., 1998). Previous work described the off-axis volcanic and plutonic suites as alkaline magmatic suites (e.g., Meyer et al., 1996), but due to the sensitivity of the alkalis (Na_2O and K_2O) to alteration, the alkaline nature of the magmatism is disputable. Because of the geotectonic implications associated with the term "alkaline magmatism," we refrain from using this term and rename the magmatic units on Masirah according to their field relations and petrography (see Section 3 for details).

Peters (2000) proposed that the oceanic crust exposed in the Upper and Lower nappes on Masirah formed at a MOR in the Late Jurassic (Upper Tithonian, ca. 150 Ma), which, due to the thin nature of the crust, was inferred to be at a low melt-supply spreading-segment end near a transform fault. They argued that this "Jurassic MOR" sequence was subsequently affected by an intra-oceanic rifting event accompanied by off-axis OIB-like "Cretaceous alkaline" magmatism in the mid-Cretaceous (Hauterivian-Aptian, ca. 123–130 Ma). This later event was inferred to be responsible for: (a) the eruption of lavas interbedded with sediments of the Maghilah Unit; (b) the formation of seamount volcanoes on top of MORB lava in the Lower Nappe; (c) the intrusion of gabbro-dolerite-granite plutons in the Upper Nappe; (d) the formation of a new sheeted dyke complex that roots in

the mantle; and (e) the localized denudation and uplift of deeper ophiolite units (i.e., mantle and gabbro) that were subsequently covered unconformably by lava and sediments of the Kalban Unit (Immenhauser, 1996; Marquer et al., 1998; Meyer et al., 1996; Peters, 2000; Peters & Mercolli, 1997, 1998). The Swiss model was informed by the dominant models of oceanic lithosphere at the time, and observations that did not fit the Penrose layer-cake model (e.g., mantle, intruded by dyke swarms and gabbroic plutons, exposed at the seafloor) were interpreted to result from later tectono-magmatic events, unrelated to the initial seafloor spreading. Subsequent oceanic research has, however, shown that features such as thin, discontinuous, or "missing" magmatic crust may be commonplace along modern slower-spreading MORs (e.g., Cannat, 1993, 1996; Dick et al., 2003; Escartín et al., 2008; Sauter et al., 2013). Therefore, these new insights justify a re-evaluation of the geological complexities of the Masirah ophiolite.

3. Field Relations

To examine the evolution of magmatism at the Masirah paleospreading ridge, we abandon the previous "Jurassic MOR" and "Cretaceous alkaline" definitions. Here, we present a revised grouping of the lava, dyke and gabbro (sensu lato) occurrences based on field relations and petrography, making no a priori assumptions about the geochemical characteristics of any particular suite or rock unit (Figure 3; studied locations in Figure 2). We follow the previously determined nappe structure and crustal stratigraphy (Peters, 2000) with the exception of the various tectonically dismembered mantle outcrops on Masirah (shown in Figure 3 as "out-of-sequence mantle"). These mantle exposures are geologically complex and occur alongside lava and sediments. Their relation to the Upper and Lower Nappes is poorly constrained in the field and, in our view, overinterpreted, being variably described as the result of post-emplacement tectonic juxtaposition of the Upper Nappe (mantle) and Lower Nappe (lavas and sediments; e.g., Marquer et al., 1995; Peters et al., 1995), or as lava and sediments directly deposited on the exhumed mantle (all Lower Nappe; e.g., Immenhauser, 1996; Marquer et al., 1998; Meyer et al., 1996).

3.1. Lavas

(L1) The "axial lavas" form the main lava exposures (by surface area) and occur at the highest stratigraphical position of the contiguous magmatic crustal sequence, where they overly a sheeted dyke complex and are overlain by deep-marine sediments of the Maghilah Unit (Figure 3 and Figure A1 in Supporting Information S1). Where preserved, pillow lava (25 cm–1.5 m, typically 50–100 cm) have a characteristic centimeter-thick pale green crust and often contain abundant plagioclase and olivine phenocrysts (0–20 vol%, 0.5–4 mm). Inter-pillow material consists of fine hyaloclastites and breccias. No glasses were observed, although it is not clear whether this is due to weathering or alteration. Higher up in the succession, the average size of pillow lava decreases to 30–50 cm, although 1–1.5 m pillows still occur. Here, the pillow matrix and crust display a conspicuous red color, and plagioclase phenocrysts and zeolite-calcite amygdales become more common, with subordinate amounts of olivine and pyroxene phenocrysts. Due to their occurrence in the vicinity of the MMT throughout the island, their red color and amygdale growth has been interpreted as a late feature associated with the nappe thrusting and emplacement of the ophiolite (Peters et al., 1995).

(L2) The "seamount lavas" are exposed over ~2.5 km^2 near Shi'inzi in the north of the island, where they overly pillow lava resembling axial lava (although deeper units of an axial crustal section are not exposed) and are in tectonic contact with a mantle section (Figure 2; Meyer et al., 1996). This area contains remnants of volcanic edifices, stock-like subvolcanic intrusions in pillow lavas, vent agglomerates, pyro- to epiclastic breccia deposits, as well as pillow lava and sheet flows intercalated with deep-marine sediments (Meyer et al., 1996; Peters & Mercolli, 1997). Together, they are interpreted as remnants of submarine seamount volcanoes that originally stood up to a few hundred meters high and a few kilometers in diameter (Meyer et al., 1996). Lithologies range from basalts to differentiated trachytes and rhyolites. Basalts are most common, occurring as dykes and lava and containing similar amounts of olivine, less clinopyroxene, and more plagioclase, Fe-Ti oxides and apatite compared to axial lava. Additionally, they may contain small amounts of hornblende and biotite (Meyer et al., 1996). Trachytes and rhyolites form fine-grained, light orange-brown stocks and dykes and contain sodic-plagioclase, alkali-feldspar and quartz, with small amounts of black amphibole needles and biotite present in some rocks (Meyer et al., 1996). The seamount lava have a reddish-brown coloration due to finely dispersed Fe-hydroxides and are rich (25 vol% on average) in calcite-zeolite amygdales (Peters et al., 1995).
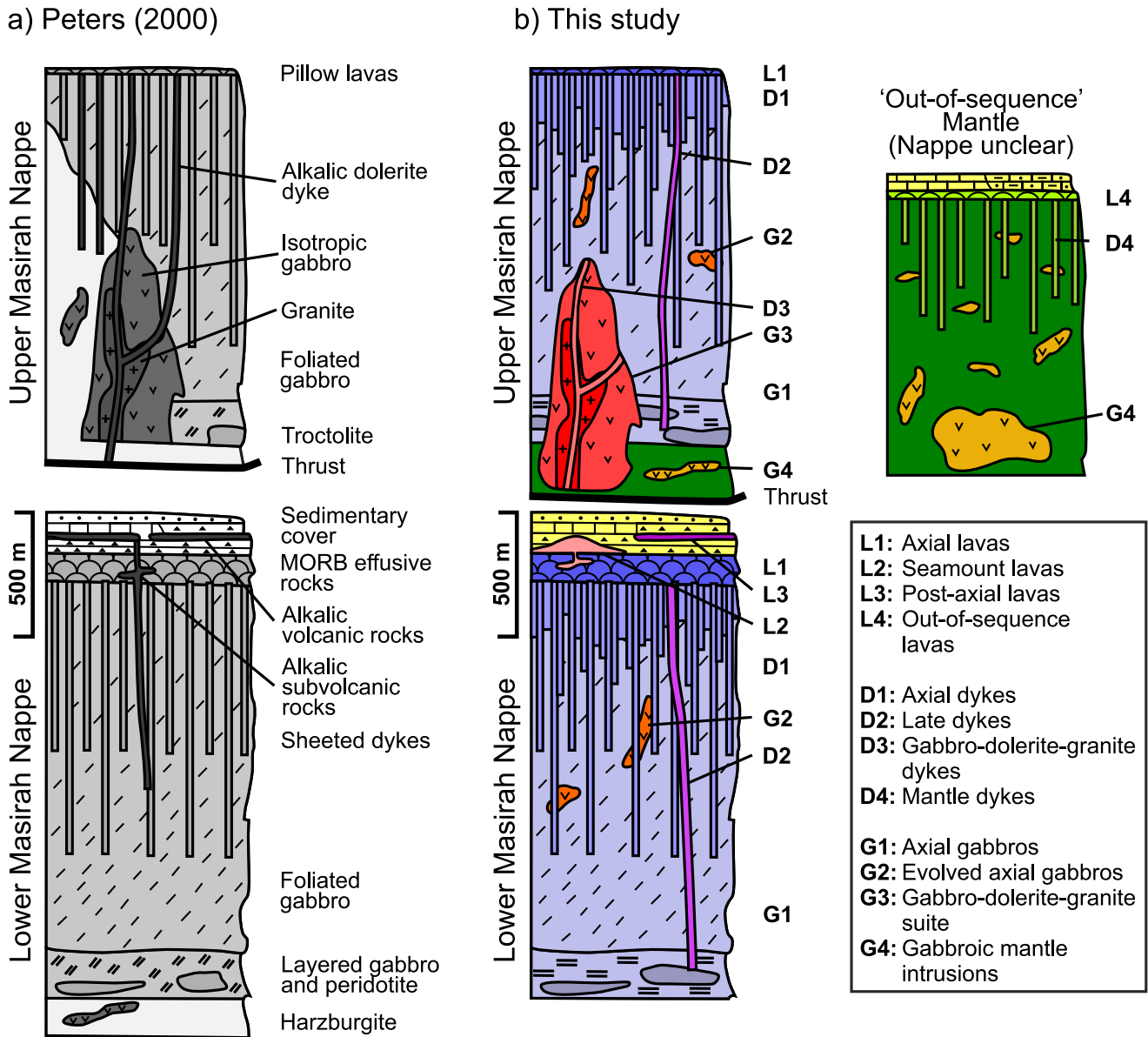
Figure 3. (a) Composite lithostratigraphic section through the lower and upper nappes of the Masirah Ophiolite by Peters (2000). (b) A revised cartoon illustrating the occurrence and relationships of the lava (L), dyke (D) and gabbro (G) groups identified in this study based on field observations. Mantle outcrops that are tectonically complex and lack direct evidence for contiguity with either nappe have been drawn in a separate "out-of-sequence" mantle column. Other key differences include the thinning of the crust in the Upper Nappe in (a), for which we found no direct evidence for or against the interpretation that this thinning was primary (i.e., on-axis); the presence of a "true" sheeted dyke complex underlying the lava in (b); and layering and foliation in the lower gabbros oriented parallel to the crust-mantle boundary in (b). These aspects will be discussed in more detail in a future publication on the architecture of the Masirah lithosphere.

(L3) The "post-axial lavas" are interbedded with the deep-marine sediments of the Maghilah Unit (Immenhauser, 1996; Meyer et al., 1996). They overlie an estimated 10–30 m of micrites and ribbon cherts deposited concordantly on the Lower Nappe axial lavas, and are interlayered with ribbon cherts, shaley interbeds, nodular cherts and turbidites of ophiolite material (Immenhauser, 1996). These lava are mainly dark-brown/green unsorted pillow breccias with local occurrences of small lava flows, and have a similar mineralogy and amygdale content as the seamount lava (Meyer et al., 1996). The Maghilah Unit is laterally variable, and postaxial lava does not occur everywhere (e.g., in Wadi Haql; Immenhauser, 1996).

(L4) The "out-of-sequence lavas" overlie rock-units other than a sheeted dyke complex or sediments (primarily mantle, as well as gabbro and sheeted dykes in some cases; Meyer et al., 1996). These pillow lava and pillow

breccias are petrographically similar to the seamount lava and mainly occur as scattered, mostly fault-bounded outcrops along the southwestern coastal Kalban plain, as well as near Shi'inzi in the north and at Jabal Suwayr in the south (Figure 2; Meyer et al., 1996). They occur near tectonically dismembered outcrops of mantle and gabbro, although their primary relationships have often been obscured. They are commonly overlain by the sedimentary Kalban Unit, which varies laterally from shallow-marine platform carbonates, to hemi-pelagic limestones and cherts interbedded with platform detritus, to pelagic radiolarian cherts (Immenhauser, 1996). At and around Jabal Suwayr (Figure 2 and Figure A1 in Supporting Information S1), a section of horizontal lava directly overlying the mantle is marked by an erosional surface and overlying platform carbonates. The base of this succession is marked by a red breccia of variable thickness (tens of centimeters to meters) with clasts of basalt, dolerite, gabbro and epidosite and a clay-rich matrix, while the overlying beds of the carbonate sequence contain angular to subangular clasts (1–50 cm, 10 cm on average) of aphyric and plagioclase-phyric basalt and gabbro. These observations were interpreted to record the exhumation of the mantle and rapid local uplift of the seafloor to sea-level, followed by subaerial erosion, carbonate platform formation and ultimately platform drowning due to renewed subsidence (Immenhauser, 1996; Meyer et al., 1996; Peters et al., 1995).

3.2. Dykes

(D1) The "axial dykes" are part of the contiguous magmatic crustal sequence and occur at the lithostratigraphic level between the gabbros and lava (Figure 3). They mainly form subparallel dyke swarms with gabbroic screens, with dyke-to-gabbro proportions that vary from 0% to 100% over hundreds of meters of crustal stratigraphy (Figure A1 in Supporting Information S1). Occurrences of "true" sheeted dyke complex (i.e., 100% dyke-in-dyke intrusion) are generally limited to the uppermost part of the sequence where the dykes are overlain by lava (estimated several hundred meters thick, but thinner than the overall gabbro-dyke transition). Dykes commonly crosscut gabbro and have well-developed chilled margins, whereas gabbro intruding pre-existing dykes is only rarely observed. Dykes are generally ~0.8–1.5 m wide and can be crystal-rich, containing plagioclase (up to 50%, 0.1–3 cm) and to a lesser extent pyroxene and olivine (~0%–5%) phenocrysts and glomerocrysts. In the studied locations, the oldest group of dykes are typically gray, aphyric to plagioclase- and pyroxene-phyric dolerites, which are crosscut by black aphyric dolerite and pale green, aphyric to slightly plagioclase- and pyroxene-phyric dolerites, although crosscutting relationships opposite to this general trend were also observed.

(D2) A group of "late dykes" is defined as any dyke that clearly crosscuts the main generation of axial dykes or isolated dykes that crosscut the axial lava or axial lower crust. Late dykes can occur at all stratigraphic levels of the magmatic crust and are often aphyric. In most respects, they are similar in field appearance to the axial (D1) and mantle dykes (D4).

(D3) The "gabbro-dolerite-granite dykes" are dykes that are associated with the intrusive gabbro-dolerite-granite suite (G3). Some dykes crosscut this suite, whereas others show intermingling structures and backveining with their host gabbros and granites, indicating contemporaneous emplacement (Peters & Mercolli, 1997). The mineralogy of the dykes is dominated by brown hornblende with varying amounts of biotite and no clinopyroxene (Peters & Mercolli, 1997).

(D4) The "mantle dykes" consist of dyke swarms intruding sections of the out-of-sequence mantle. Their areal extent on Masirah is relatively small and tectonic dismemberment of these sections obscures their relationship with the axial crustal sequence. Outcrops are generally patchy and discontinuous (~10% outcrop) and intensely brecciated. In the more pristine outcrops, dykes display clear chilled margins and can be continuous for tens of meters (Figure A1 in Supporting Information S1). They generally crosscut any gabbroic intrusions present in the mantle, although in rare instances gabbro intrudes and stops dolerite dykes. Compared to axial dykes, mantle dykes are 0.1–2.5 m thick and mostly consist of dolerites with chilled margins. Crystal-bearing dykes are more common than aphyric dykes, with plagioclase as the most common phenocryst (generally <5%, occasionally up to 20%), sometimes accompanied by clinopyroxene (<5%), although some exclusively pyroxene-phyric dykes also occur. Despite being regionally variable, dyke trends are subparallel on a <100 m scale.

3.3. Gabbro Occurrences

(G1) The "axial gabbros" constitute the main gabbro occurrence on Masirah and form the lower crust that underlies the axial lava and dykes (Figure 3). With an estimated thickness of ~500 m, this unit consists of a series of layered gabbro and dunite at its base, overlain by magmatically foliated gabbros that grade into the sheeted dyke

complex. The basal sequence is dominated by modally layered olivine gabbro, troctolite, plagioclase-dunite and plagioclase-wehrlite, whereas gabbro (sensu stricto) is the most common lithology in the upper part of the section, occasionally containing accessory brown amphibole, Fe-Ti oxides, titanite and apatite (Figure A2 in Supporting Information S1). The axial gabbros have granular to ophitic textures and display non-pervasive (but generally consistent) magmatic lineation and foliation fabrics defined by a preferred alignment of crystal shapes (Figure A3 in Supporting Information S1). Crystal plastic deformation is sparse to absent.

(G2) "Evolved axial gabbros" occur sporadically in the upperpart of the axial gabbros (G1) and often form sub-meter veins and segregations in gabbro outcrops that are commonly crosscut by axial dyke swarms (D1). They include isotropic "varitextured gabbros," which have heterogeneous grainsizes ranging from fine to pegmatoid over distances of tens of centimeters, and contain plagioclase, clinopyroxene and occasional accessory hornblende and Fe-Ti oxides (Figures A2 and A3 in Supporting Information S1). Their textural facies resemble the "varitextured gabbro" lithostratigraphic unit described in the Semail Ophiolite (MacLeod & Yaouancq, 2000), although on Masirah these rocks notably do not form a distinct 150 m thick stratigraphic level at the top of the lower crust, as is observed in Semail. Meter-sized dykelets, pods and vein-segregations of leuco-gabbro, anorthosite, diorite and albitite, sometimes with accessory oxides, apatite, titanite and zircon, also occur sporadically in these outcrops.

(G3) The "gabbro-dolerite-granite suite" forms 0.5–3.5 km sized intrusions that mainly crosscut the crust-mantle boundary in the Upper Nappe. The dominant lithology is varitextured hornblende-oxide gabbro containing plagioclase, clinopyroxene and amphibole crystals that reach up to 10 cm (Figures A2 and A3 in Supporting Information S1). Pegmatoid gabbro segregates into veins and dykelets that back-intrude microgabbro and form irregular blocks. Subordinate occurrences of dolerite dykes (D3) and meter-sized lenses of granite, tonalite and albitite display mutual crosscutting relationships with the gabbros. Although their heterogeneous grainsize is similar to the varitextured evolved gabbros (G2), they can be distinguished by abundant hornblende that occurs as reaction rims replacing clinopyroxene (sometimes completely consuming the latter), anhedral blebs along clinopyroxene cleavage planes, and interstitial to poikilitic crystals enclosing plagioclase chadacrysts. Hornblende is often intergrown with subhedral to anhedral magnetite-ilmenite pairs (up to 5 vol%).

(G4) Isolated "gabbroic mantle intrusions" occur as dykelets, veins and meter-sized pods in mantle peridotites. They lack chilled margins and range in proportion from virtually absent to abundant. The majority are pods of varitextured or pegmatoid hornblende-oxide gabbro (meters to tens of meters in size) as well as less common meter-sized leucocratic and granitic dykes, comparable to the lithologies of the gabbro-dolerite-granite suite (G3). They contain similar textures of brown amphibole replacing clinopyroxene, although the reaction has typically progressed to a lesser extent. The intrusions are crosscut by mantle dykes (D4) where they occur although the varitextured gabbro intrudes and stops the dolerite dykes in rare instances. A smaller proportion of the mantle intrusions consist of olivine gabbro with similar granular to ophitic textures as the axial gabbros (G1). Some mantle intrusions have characteristics overlapping with both axial gabbros and the gabbro-dolerite-granite suite, forming meter-scale varitextured and pegmatoid pods of granular to ophitic gabbro and olivine gabbro containing only minor amounts of brown amphibole and Fe-Ti oxides (Figure A3 in Supporting Information S1).

4. Analytical Methods

A detailed description of the analytical methods is provided in Supporting Information S1. A total of 47 samples were selected for whole-rock (WR) geochemical analysis (10 axial lavas, 2 seamount lavas, 13 axial dyke margins, 16 mantle dyke margins, and 6 of the geochronology samples, see below). Trace element compositions of a larger group of 65 axial and mantle dykes were analyzed using a portable X-ray fluorescence (pXRF) spectrometer at Cardiff University. Samples for WR chemistry were prepared into fused beads using standard techniques and were analyzed for major elements on a PANalytical Axios Wavelength Dispersive X-ray fluorescence (XRF) spectrometer and for trace elements on a Resolution 193 nm Excimer laser from Applied Spectra connected to an Agilent 7700 Q ICP-MS (LA-ICP-MS) at Stellenbosch University. Each trace element datum represents an average of two LA-ICP-MS analyses with a spot-size of 104 µm. Calibration was achieved using standard-sample bracketing with NIST 610 reference material every 15 to 20 samples and the accuracy of the laser ablation was monitored by repeat analyses of BHVO-2G and BCR-2G (glasses) and BHVO-1 and BCR-2 (fused beads from powders) as well as two previously analyzed lava from the Semail Ophiolite. Data were processed with the Norris Scientific LADR software package using Al_2O_3 as an internal standard (Norris &
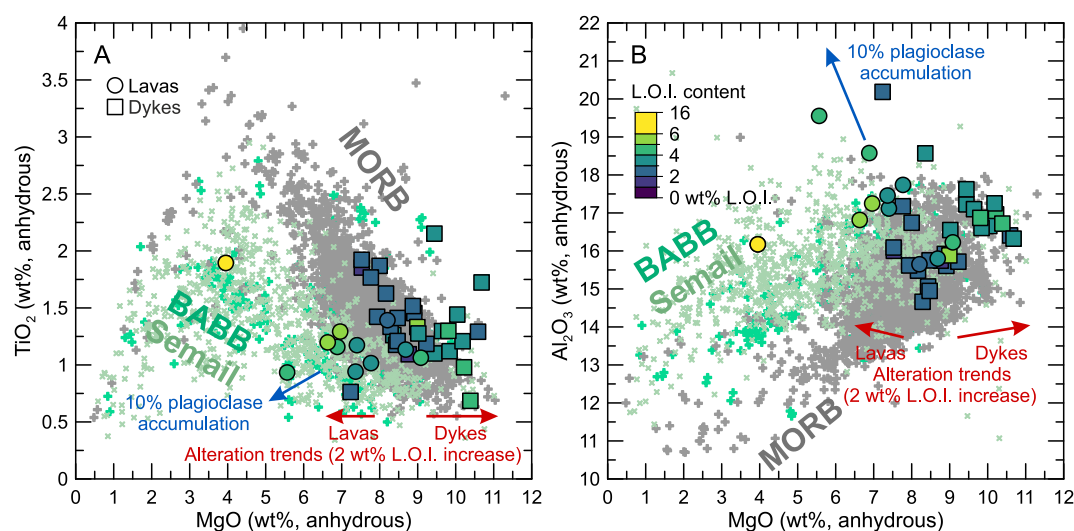
Figure 4. Anhydrous differentiation trends for the Masirah lava and dykes compared to MORB, BABB and the subduction-setting Semail ophiolite. Most Masirah lava and dykes follow the MORB trends for TiO_2 versus MgO (a) and Al_2O_3 versus MgO (b). Deviations from MORB trends in several samples can be accounted for by either plagioclase accumulation, resulting in an increase in Al_2O_3 and a decrease (by dilution) of TiO_2 and MgO, or alteration trends, resulting in elevated Al_2O_3, a loss of MgO in the lava and an increase of MgO in the dykes. Plagioclase accumulation vectors represent 10% crystal content (with a composition of 32 wt% Al_2O_3 and 0 wt% MgO and TiO_2) and alteration vectors for dykes and lava represent the change in composition for an Increase of 2 wt% L.O.I. (derived by a linear regression of major elements vs. L.O.I.). MORB and BABB data from Gale et al. (2013) and Semail data from MacLeod et al. (2013).

Danyushevsky, 2018). Combined precision and accuracy of trace elements were generally better than 10%. To demonstrate that our observed trends are representative for the whole ophiolite, WR compositions from this study are compared with a compilation of previously published and unpublished geochemical WR data for Masirah, categorized according to sample type, location, setting and field relations in a "MasirahDB" database, following our classification scheme described above (Table S4 in Supporting Information S2 for further details. Data sources: Abbotts, 1979; Mahoney et al., 1998; Meyer et al., 1996; Nägler & Frei, 1997; Peters & Mercolli, 1998; Peters et al., 1995; unpublished data from the University of Bern Masirah Island mapping project).

Nine samples (7 evolved axial gabbros and dykes and 1 intrusive anorthosite from Masirah, as well as 1 mantle intrusion from Ra's Madrakah on the mainland) were selected for high precision zircon U-Pb geochronology at the BGS NIGL facilities in Keyworth. Single zircons were isolated from the rock material using Selfrag© and standard mineral separation techniques. To minimize the effect of Pb-loss, selected zircons were subjected to chemical abrasion to remove damaged parts of the crystal that likely experienced open-system behavior (Mattinson, 2005). Uranium-Pb isotopic compositions of individual zircons were determined by ID-TIMS using a ^{202}Pb-^{205}Pb–^{233}U–^{235}U mixed-spike and data reduction was carried out using UPb Redux (McLean et al., 2011). All dates were corrected for initial Th/U disequilibrium and the uncertainties on the tracer and blank compositions were propagated into the measurement uncertainty. The blank contribution was determined by monitoring ^{204}Pb and assuming that all common Pb (Pb_c) was blank-derived.

5. Geochemical Results

The lava and dyke anhydrous major element whole-rock compositions are basaltic, relatively primitive (Mg# = 0.61–0.74) and variably altered (loss on ignition, L.O.I. = 1.3–13.1 wt%; Table S1 in Supporting Information S2). Seamount lava 18MM365 does not reflect a melt composition (73 wt% SiO_2, 22 wt% CaO, all other major elements <2 wt%) and is disregarded in further discussion and figures. All other samples fall on MORB differentiation trends, consistent with a dry MORB-like origin and different from back-arc basin basalts (BABB) and ophiolites formed in supra-subduction zone settings (e.g., Semail ophiolite; Figure 4). Major element trends are disrupted to some degree by crystal accumulation and hydrothermal alteration (further details provided in Supporting Information S1). The following geochemical characterization focuses on immobile trace elements (TiO_2, Zr, Y, Nb and the rare earth elements, REE) that largely remained unaffected by this disruption. We avoid

using alkalinity as a magmatic proxy since the geochemical parameters on which this definition is based ($Na_2O + K_2O$) are affected by alteration.

Most of the axial lava (L1) and dykes (D1) have MORB-like TiO_2, Zr, Y and Nb contents (Nb/Y < 0.8, "low-Nb") and variable rare earth element (REE) compositions that range from D-MORB (La_N/Sm_N < 0.8, normalized to primitive mantle; McDonough & Sun, 1995) to E-MORB (La_N/Sm_N > 1.5, definitions from Gale et al. (2013); Figures 5a–5d). Despite a large degree of overlap, the axial dykes sampled for this study are slightly more enriched (La_N/Yb_N = 0.85–5.70, average 2.19, n = 25) than the axial lava (La_N/Yb_N = 0.32–4.71, average 1.33, n = 18). Trace element compositions of the axial dykes occurring as the dyke swarms in the gabbro-dyke transition mostly overlap with the "true" sheeted dykes but also include several compositions that are more enriched. We found no consistent relationship between lava and dyke composition and physical appearance (crystal content and color) or sampling location. Due to more extensive and complete exposures of axial dykes and lava in the Lower Nappe compared to the Upper Nappe, the latter is less well represented in MasirahDB for these units. Nevertheless, the available data suggest that the range of axial melts in the Upper Nappe (notably in the Sur Masirah area) extends to more enriched compositions than the Lower Nappe.

The seamount lava (L2), gabbro-dolerite-granite dykes (D3), post-axial lava (L3) and out-of-sequence lava (L4) are enriched in TiO_2, Zr, Nb (Nb/Y > 0.8, "Nb-enriched") and LREE (La_N/Yb_N of 4.85–11.84, average 8.28, n = 5; Figure 5) with respect to the Masirah axial lava and dykes as well as modern MORB. Magmatically differentiated seamount lava have elevated Zr (~1,200 ppm), Nb (~180 ppm) and Y (~120 ppm), whereas TiO_2 contents drop below 0.5 wt% after an initial increase, consistent with differentiation beyond Fe-Ti oxide saturation.

Despite these compositional distinctions between the MORB-like, low-Nb axial lava and dykes on the one hand, and the Nb-enriched seamount lavas, gabbro-dolerite-granite dykes and post-axial lava on the other, there is overlap between these two groups (Figure 5c). A minority of axial lava and dykes have elevated Nb contents (Nb/Y > 0.8, "Nb-enriched"), typically accompanied by Zr, TiO_2 and LREE enrichment. Vice versa, some seamount lava and gabbro-dolerite-granite dykes have low-Nb compositions, resulting in overlap with the most enriched axial lava and dykes. Furthermore, the late dykes (D2) and mantle dykes (D4) each span a wider range of trace element compositions, overlapping almost entirely with both MORB-like and low-Nb compositions as well as LREE-enriched and Nb-enriched compositions (e.g., mantle dyke La_N/Yb_N ranges 0.73–8.66, average 3.14, n = 16).

To establish whether there are systematic temporal changes in melt composition, geochemical data were combined with dyke crosscutting relationships observed in the field. For this purpose, the WR data were supplemented by pXRF data, which was found to accurately reflect WR Zr/Y, a useful proxy for LREE enrichment (Figure A8 in Supporting Information S1 and Table S2 in Supporting Information S2 for details). We found no evidence in support of two distinct geochemical groups or a simple evolution of geochemistry through time. Instead, early and late dykes span similar ranges in trace element compositions, with depleted dykes crosscutting enriched dykes and vice versa (Figure 6). Additionally, enriched dykes crosscutting depleted dykes is the most commonly observed relationship in our sample set, and dykes with the strongest trace element enrichments (Zr/Y, Nb/Y, and LREE) always belong to the latest generation in an outcrop, sometimes with an anomalous orientation but often sub-parallel to the regional dyke trend. Although the axial lava stratigraphy was not studied at the level of detail required to identify geochemical trends, our and MasirahDB data show the occurrence of both enriched and depleted lava at various stratigraphic intervals, from which we conclude that the D-MORB to E-MORB lava are interbedded. These observations are consistent with a model where the melts delivered to the Masirah paleoridge axis have varying compositions along a continuum that on the whole becomes more enriched over time.

6. Geochronology: High-Precision Zircon Ages

The field relations, petrography and whole-rock chemistry of the seven evolved axial gabbros and dykes selected for geochronological analyses indicate that they are coeval with the axial crustal sequence (2 in the Lower Nappe, 5 in the Upper Nappe, sample locations in Figure 2). Two additional samples were analyzed: an intrusive anorthosite that crosscuts (i.e., postdates) the axial crust of the Lower Nappe, and a felsic intrusion from the mantle section at Ra's Madrakah on the mainland (relative age unknown, see the Supporting Information S1 for detailed sample descriptions). U-Pb zircon data are reported in Table S3 of the Supporting Information S2 and plotted in Figure 8 and Figures A11 and A12 in Supporting Information S1. Seven zircon analyses with a
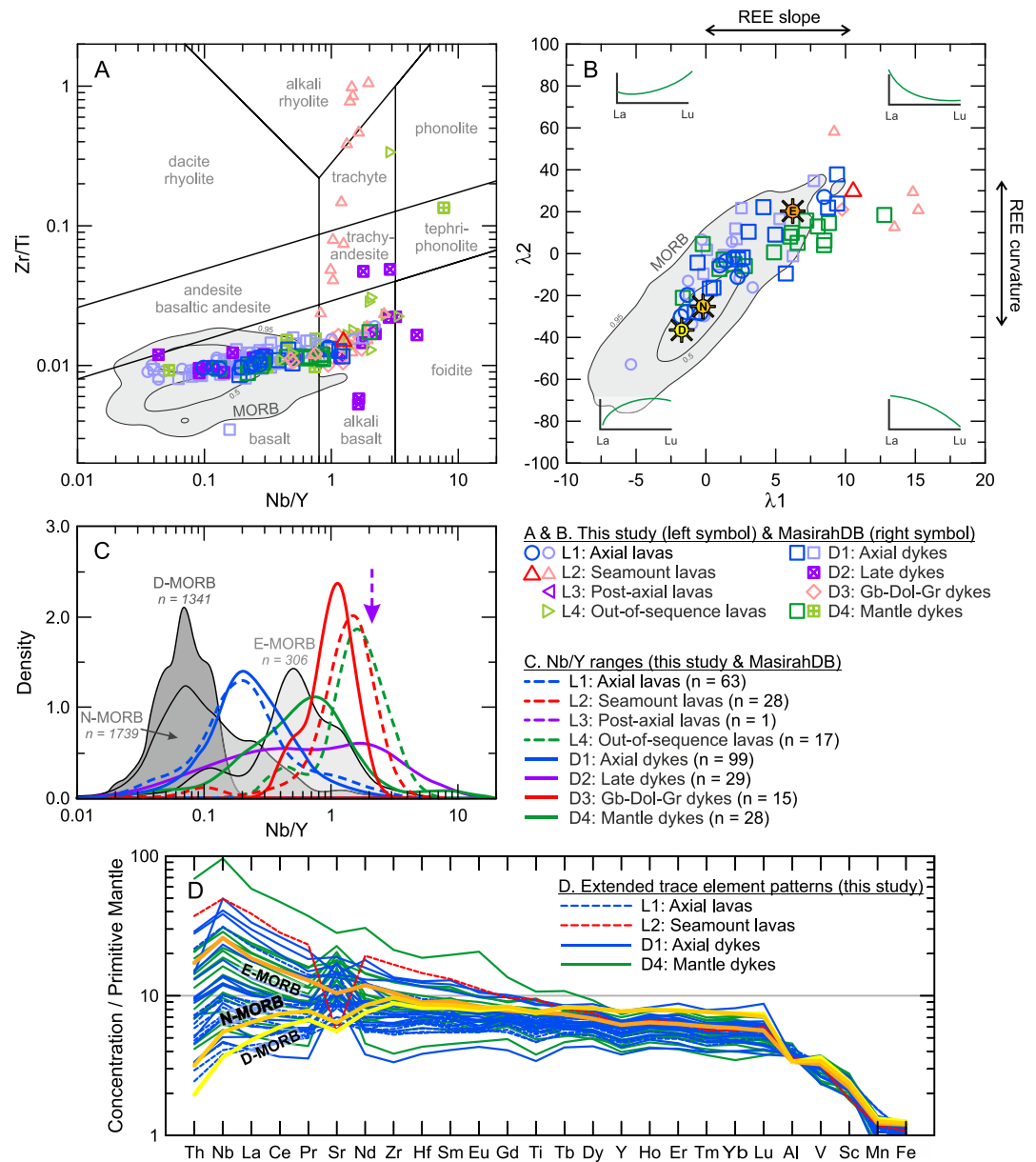
Figure 5. Masirah dyke and lava trace element compositions. (a) Nb/Y versus Zr/Ti plot (after Pearce (1996)). (b) Lambda-plot for REE shape patterns (after O'Neill (2016)). (c) The range of Nb/Y in the Masirah dykes and lava shown as kernel density estimation (KDE) curves calculated using ^{10}log(Nb/Y). The purple arrow indicates the composition of the single post-axial lava datum. Ranges for present-day N-MORB (all MORB > 500 km from a plume-fed hotspot), D-MORB (all MORB with La/Sm$_N$ < 0.8) and E-MORB (all MORB with La/Sm$_N$ > 0.15) are shown for comparison (data and definitions for N-, D-, and E-MORB from Gale et al. (2013), back-arc basin data are excluded). (d) Primitive mantle normalized extended trace element patterns. Normalizing values from McDonough & Sun (1995) and trace element order after Pearce and Parkinson (1993). MORB fields in (a) and (b) are based on kernel density contours enclosing 95% and 50% of MORB data compiled by Gale et al. (2013) (excluding back-arc basins and MOR segments <500 km from a plume-fed hotspot). Average compositions of D-MORB, N-MORB, and E-MORB from Gale et al. (2013) are shown in (b) (respectively labeled D, N, and E) and (d).

significant blank contribution relative to the sample size (Pb*/Pb$_c$ < 10, with Pb* indicating radiogenic Pb) were not considered in further discussion of the data and the remaining 42 analyses had 0.2–1.1 pg Pb$_c$ (0.42 pg on average) and a Pb*/Pb$_c$ ratio of 10 or greater (10–358, average = 53). All dates plot on (or near) ^{207}Pb/^{235}U-^{206}Pb/^{238}U concordia. Individual ^{206}Pb/^{238}U zircon ages of the samples from the Upper Nappe are younger (ranging 131.91 ± 0.08 to 130.47 ± 0.17 Ma; n = 24) than the ages of samples from the Lower Nappe
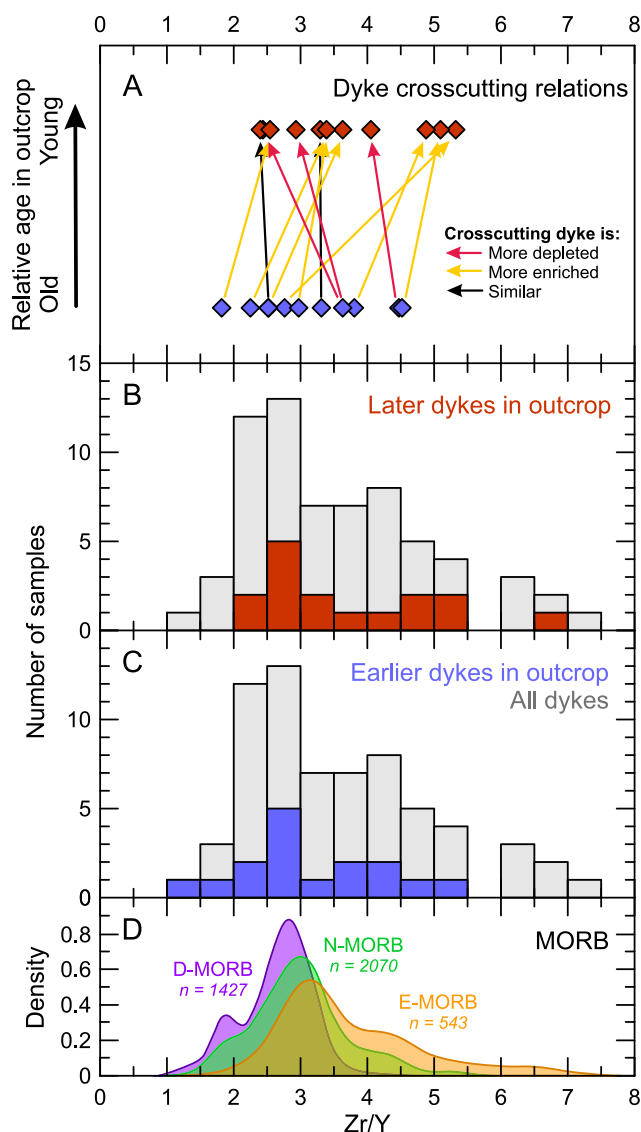
Figure 6. (a) Trace element compositions and crosscutting relationships for 12 pairs of dykes show that trace element enriched magmatism was contemporaneous with depleted magmatism. Nevertheless, enriched dykes more commonly crosscut depleted dykes than the other way around, and dykes with a younger relative age (b) are on average more enriched than dykes with an older relative age (c). Dykes with no crosscutting relationships are shown in gray. (d) Zr/Y compositional ranges of present-day N-MORB, D-MORB, and E-MORB as KDE curves for comparative purposes (Gale et al., 2013).

(ranging 135.16 ± 0.11 to 134.73 ± 0.10; $n = 13$) with the exception of one zircon (131.22 ± 0.12 Ma), whose younger age was attributed to Pb-loss (see Supporting Information S1). When examining the age variations within individual samples, four samples are characterized by statistically significant $^{206}Pb/^{238}U$ age clusters (two of which also include outliers), whereas the remaining three display overdispersion in their zircon ages. Nevertheless, since the intra-sample age range in these samples is small (typically <0.4 Ma) relative to the age difference between the two nappes, the nappe ages are considered robust (see Supporting Information S1 for details). The two remaining samples, which intrude the Masirah Lower Nappe and the mantle section at Ra's Madrakah, have ages spanning 66.52 ± 0.04–65.80 ± 0.06 Ma ($n = 4$). The younger ages of these intrusions closely agree with the proposed obduction age of the Eastern Oman Ophiolites sometime between the late Maastrichtian and early Paleocene (Gnos et al., 1997) as well as small-scale magmatism in the Batain region (e.g., Gnos & Peters, 2003), suggesting that ophiolite emplacement was accompanied by small-scale melting.

7. Discussion

7.1. Chemical Evolution of Masirah

This study finds that the different lava and dyke groupings on Masirah are characterized by partially overlapping ranges of trace element compositions that together form a continuum spanning the MORB array (from D-MORB to E-MORB) and extending to more enriched compositions (Figure 5). The axial lava and dykes were formed by a diverse range of melt compositions, including Nb-enriched melts. Nevertheless, despite a considerable and seemingly random variation within each defined subgroup, the latest dykes (based on cross-cutting relationships) are generally more Nb/Y and LREE-enriched, as are the units that postdate the axial sequence (i.e., seamount lavas, post-axial lava and the gabbro-dolerite-granite dykes; Figure 6). The observed geochemical overlap suggests that the magmatic processes that formed the various lava and dyke units are closely intertwined, consistent with a transitional magmatic system where the range of melt compositions becomes more enriched over time. This departs from the previous model for Masirah, where the axial lavas, dykes and gabbros formed during the main crustal accretion event at a MOR, followed by a separate, chemically distinct, intraplate magmatic event responsible for the eruption of seamount and post-axial lava and the intrusion of late dykes, mantle dykes and the gabbro-dolerite-granite suite (Peters, 2000).

The primitive nature of the lava and dykes (in terms of MgO, Cr, Ni, and Mg#) combined with the limited thickness of the gabbroic lower crust argues for a subordinate role for magmatic differentiation in generating the observed trace element variations. Instead, the enriched trace element compositions can be produced by a combination of a reduced degree of melting and a greater contribution of an enriched mantle source. We demonstrate this by plotting REE compositions and two simple non-modal accumulated fractional mantle melting models in a lambda-parametrization plot, in which subtle nuances in REE slope and curvature become more readily identifiable (Figure 7a; O'Neill, 2016). The melting models (from O'Neill (2016)) were calculated for the spinel stability field (10 kbar) and are shown as traces as a function of the degree of melting (F%). Both models use spinel-lherzolite as the source and melt compositions are calculated using constant melting reactions and crystal/melt partition coefficients (O'Neill, 2016 and references therein). The first model (purple) shows the resulting REE patterns of the melt for a source with a primitive mantle REE composition (McDonough & Sun, 1995) and the second model (pink) for a source with a depleted MORB mantle REE composition (Workman & Hart, 2005). Figure 7a illustrates that the shape of the lava and dyke REE patterns can be modeled by various degrees of shallow melting of a variably enriched source. Notably, the LREE-
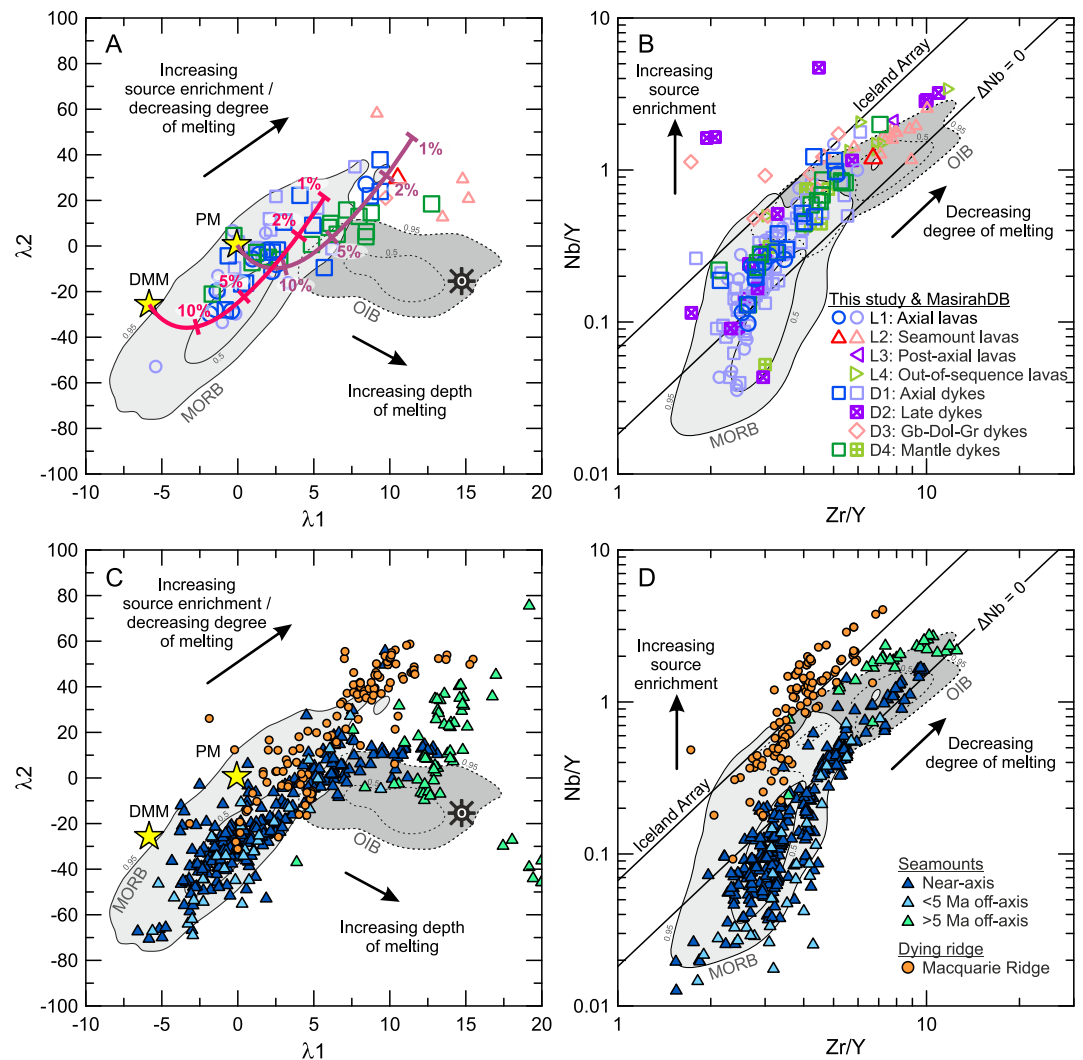
Figure 7. (a) Lambda-plot for REE shape patterns after O'Neill (2016). Melting curves are based on an accumulated fractional melting model of spinel lherzolite at 10 kbars (see text). Depleted MORB Mantle (DMM) composition from Workman and Hart (2005) and Primitive Mantle (PM) composition from McDonough and Sun (1995). (b) Nb/Y versus Zr/Y trace element diagram (excluding data with MgO < 5 wt%) after Fitton et al. (1997), showing the effects of source enrichment versus degree of melting. Panel (c and d) shows the same plots with lavas from seamounts that formed on oceanic lithosphere of varying ages (near-axis: Anderson et al., 2021; Geshi et al., 2007; Niu & Batiza, 1997; <5 Ma off-axis: Hall et al., 2006; Janney et al., 2000; >5 Ma off-axis: Davis et al., 2002; Hirano et al., 2006; Janney et al., 2000) and lavas from a dying spreading ridge at Macquarie Island and Macquarie Ridge (compiled by Jiang et al. (2021)). MORB and OIB fields are based on kernel density contours enclosing 95% and 50% of respectively MORB data (compiled by Gale et al. (2013), excluding back-arc basins and MOR segments <500 km from a plume-fed hotspot) and OIB data from Réunion, Mauritius, Crozet and Amsterdam Island (Albarède et al., 1997; Breton et al., 2013; Doucet et al., 2004; Moore et al., 2011; Paul et al., 2005, 2007). Average OIB composition (black sun symbol labeled O) from Sun and McDonough (1989) is shown in (a) and (c).

enriched Masirah lava and dykes have relatively high λ2 values and are therefore different from plume-fed OIBs and seamounts that erupted on old and thick oceanic lithospheres (Figure 7c). High λ2 values represent a lack of depletion in heavy REE (HREE), typical for melting in the presence of garnet, therefore ruling out a major role for deep melting in the garnet stability field.

To distinguish between the effects of degree of melting and mantle source, we examined co-variations between Nb/Y and Zr/Y. These proxies were originally developed for Icelandic basalts (Fitton et al., 1997), although Fitton (2007) showed that the Iceland array in their diagram has a global significance and can be used to identify
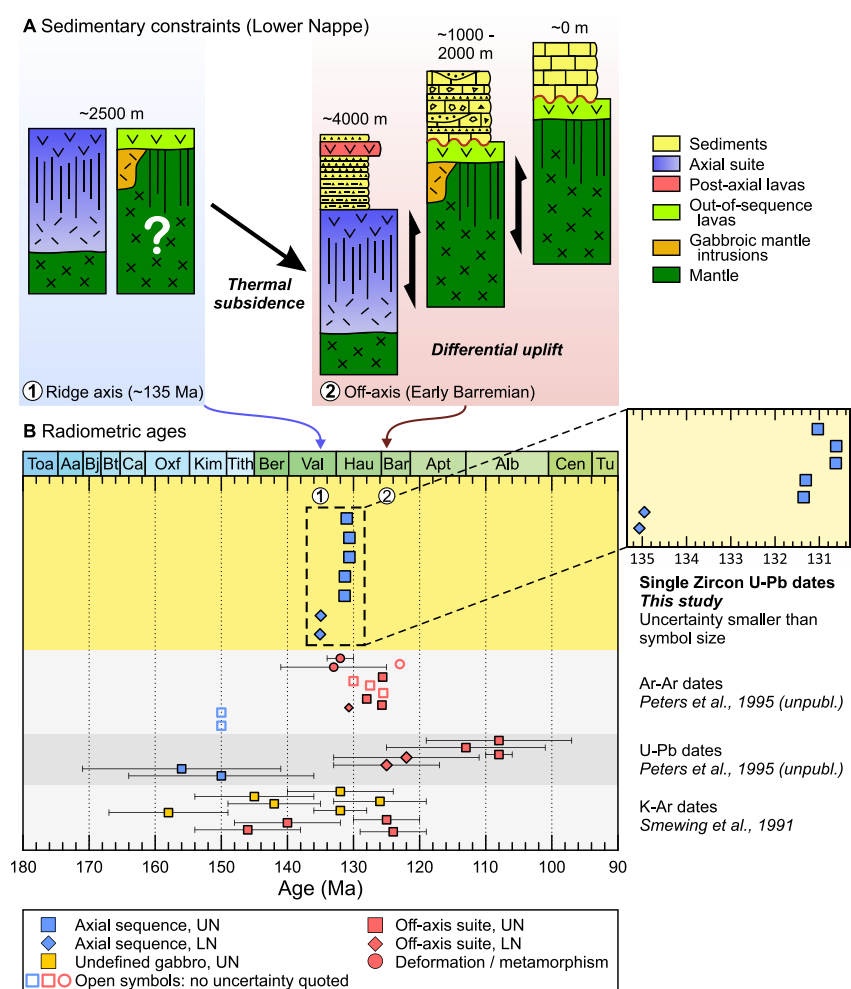
Figure 8. (a) Overview of the sedimentary constraints on the evolution of the Masirah Lower Nappe with approximate depths below sea level indicated. Off-axis thermal subsidence to below the CCD is followed by the eruption of post-axial lava (pink) and differential uplift, with some parts of Masirah recording continued sedimentation below the CCD, whereas other parts are uplifted to sea level. The timing of the exhumation of the mantle and the eruption of out-of-sequence lava is not constrained. (b) Overview of geochronological data from this study and the literature. Uncertainty for data from this study and some unpublished Ar-Ar ages is smaller than the symbol sizes. Open symbols represent ages without a quoted uncertainty. The timing of the events illustrated in the top-panel is indicated by numbers 1 and 2. Stratigraphic geological timescale from the International Commission on Stratigraphy (Cohen et al., 2013; updated v2023/06); UN = Upper Nappe, LN = Lower Nappe, Toa = Toarcian, Aa = Aalenian, Bj = Bajocian, Bt = Bathonian, Ca = Callovian, Oxf = Oxfordian, Kim = Kimmeridgian, Tith = Tithonian, Ber = Berriasian, Val = Valanginian, Hau = Hauterivian, Bar = Barremian, Apt = Aptian, Alb = Albian, Cen = Cenomanian, Tu = Turonian.

enriched mantle sources in MORB, mantle plume-fed oceanic islands, and off-axis seamounts. Low pressure fractional crystallization has no significant effect on these ratios for MgO > 5 wt% and varying degrees of melting results in covariation along linear arrays parallel to the Iceland array (Figure 7b). Any vertical offset from this array, expressed as excess or deficit in log units of Nb (ΔNb) from the reference line marking the lower bound of the Iceland array, arises from source heterogeneity (Fitton et al., 1997). Figure 7b shows that the Masirah axial dykes and lava are derived from a heterogeneous source with varying degrees of Nb-enrichment. Furthermore, the data suggest that the Nb-enriched lava and dykes that postdate the axial sequence (i.e., the former "alkaline suite") can be formed by lower degrees of melting of the enriched component that also contributed to the formation of axial E-MORB. This is consistent with previous Nd-Sr-Pb isotope studies, which show that the Masirah axial melts are isotopically variable and lack an Indian Ocean "Dupal" isotope signature, instead overlapping with the present-day North Atlantic and Pacific MORB mantle source array (Mahoney et al., 1998). The E-MORB and

Nb-enriched lava and dykes partially overlap with the axial suite in isotope space and trend toward an enriched source that is isotopically close to the volcanic islands of Réunion, Mauritius, Crozet and St Paul & Amsterdam in the Indian Ocean (see Supporting Information S1 and Figure A14 in Supporting Information S1 for details; Mahoney et al., 1998; Zhang et al., 2005).

7.2. Temporal Evolution of Masirah

Our new zircon ages suggest a formation age of 135.1–135.0 Ma for axial gabbros from the Lower Nappe and 131.4–130.6 Ma for axial gabbros from the Upper Nappe, with no systematic age variations within either nappe. This contrasts with the currently accepted Upper Tithonian age (ca. 150 Ma) for the axial magmatism, based on previous work (Immenhauser, 1996; Peters, 2000). The robustness of the chemical abrasion method used in this study as well as the concordance and reproducibility of the U-Pb ages presented here suggest that it is unlikely that Pb-loss is responsible for our younger ages for the Masirah axial crust. Instead, we emphasize that the geochronologic data from previous studies do not amount to conclusive evidence for an Upper Tithonian age, but rather provide a range of possible ages spanning the Late Jurassic to Early Cretaceous.

Previous radiometric work is limited to a K-Ar study (Smewing et al., 1991) and a table of unpublished Ar-Ar and U-Pb ages obtained from various lithologies and units from both nappes during the Swiss mapping campaign (Figure 8; Peters et al., 1995). The K-Ar ages, obtained from hornblende separates from gabbros and biotite separates from granites from the Upper Nappe, range 126–158 Ma, but have low precision and it is unclear whether the axial gabbros or the gabbro-dolerite-granite suite was sampled. The unpublished Ar-Ar and U-Pb ages cannot be assessed for data quality or statistical robustness, but are nevertheless cited in the literature. Figure 8 shows that, apart from several Ar-Ar ages from the formerly designated "alkaline suite," all ages have considerable uncertainties (>>1 Ma). Further age constraints were derived from microfossil assemblages in the sediments overlying the axial lava. The oldest Maghilah Unit sediments of the Lower Nappe were interpreted to have a Tithonian or Berriasian age (ca. 145 Ma; Immenhauser, 1995, 1996) but do not contain biostratigraphic assemblages uniquely specific to the Tithonian or Berriasian (Dumitrica et al., 1997). Radiolarian assemblages from the stratigraphically oldest sediments were found to be consistent with a relatively large range of possible ages, including our 135 Ma age for the Lower Nappe (Upper Tithonian to Hauterivian in the Wadi Maghilah section and Upper Berriasian to Lower Valanginian in the Wadi Thoumi section, locations in Figure 2; Dumitrica et al., 1997). Calcareous nanofossils from the lowest stratigraphic levels of the Maghilah Unit did not provide precise age constraints due to poor preservation of the specimens (Von Salis & Immenhauser, 1997).

Based on the above, we refute the 150 Ma formation age for Masirah and establish a 135–130 Ma age for the axial magmatism. The other magmatic units on Masirah were not dated in this study, but previous work provides some age constraints. Seamount lava and post-axial lava are interbedded with pelagic sediments deposited below the calcite compensation depth (CCD), indicating thermal subsidence during transport off-axis (Immenhauser, 1996; Meyer et al., 1996). Allowing for structural and sedimentary complexities in the individual sections, the thickness of pelagic sediments separating the axial and post-axial lava was estimated to vary from ~10 m (Wadi Rasiyah) to ~30 m (Wadi Zamir/Thoumi), whereas post-axial lava are absent in Wadi Haql (Immenhauser, 1995, 1996). Biostratigraphical age constraints are limited to the Wadi Maghilah section, where post-axial lava are interbedded with ribbon cherts that yielded a short-range radiolarian assemblage of Lower Barremian age (Dumitrica et al., 1997).

Out-of-sequence lava erupted on exhumed gabbro and peridotite although there is no direct evidence to constrain whether exhumation occurred on-axis or off-axis. They are overlain by the earliest sediments of the Kalban Unit, which also have a Barremian age, based on multiple independent biomarkers from Wadi Zabil (foraminifera, radiolarians and calcareous nanofossils) and from the platform carbonates of Jabal Suwayr (foraminifera; Dumitrica et al., 1997; Immenhauser, 1995, 1996; Von Salis & Immenhauser, 1997). The Kalban Unit records different coexisting, spatially separated sedimentation environments, ranging from platform carbonates that formed near sea-level, to above-CCD hemi-pelagic sediments and sub-CCD pelagic sedimentation, with the latter two facies containing interbedded proximal to distal platform and ophiolite detritus (Immenhauser, 1996). These observations indicate substantial uplift (~3–4 km) in some parts of the ophiolite while other parts remained at sub-CCD depths. This uplift is unrelated to ophiolite obduction, which took place much later between the late Maastrichtian and early Paleocene. Subsequent platform drowning additionally required greater subsidence rates than ambient thermal subsidence, necessitating a tectonic contribution (Immenhauser, 1996). Since lava are not

interbedded with the Kalban sediments, however, there is no direct evidence that constrains whether the out-of-sequence lava predate or postdate the uplift recorded by this unit, or whether the magmatism resulted from the uplift.

Observations therefore indicate that the latest volcanic activity on Masirah occurred around the start of the Barremian (currently dated at 125.77 Ma, Cohen et al., 2013; updated v2023/06), that is, between 5 and 10 Ma after the formation of the axial suite. In contrast to the lava units, there are no precise age constraints on the intrusive gabbro-dolerite-granite suite, late dykes, mantle dykes, or gabbroic mantle intrusions. Additionally, we note that improving the calibration of the Jurassic and Early Cretaceous radiolarian biostratigraphy, as well as linking stratigraphic and absolute ages, is the subject of ongoing work (e.g., Goričan et al., 2018; Martinez et al., 2015, 2020).

7.3. A Revised Geochronological and Tectonic Model for Masirah

The magmatic units present on Masirah show an overlap in trace element chemistry, with D-MORB and E-MORB compositions occurring contemporaneously, while recording a general evolution toward E-MORB and more enriched compositions derived from lower degree melting of an enriched mantle source. Axial magmatism took place at 135 Ma (Lower Nappe) and 130 Ma (Upper Nappe) and the latest volcanic activity occurred in the early Barremian (∼125 Ma, Lower Nappe and Out-of-sequence mantle). The ages of the later unerupted dykes and plutons are not known, however, and continuous magmatism throughout this period cannot be ruled out. Sediments of the Kalban Unit provide important constraints on uplift and subsidence of parts of the ophiolite in the Barremian, although there is no evidence for a direct relationship between uplift and magmatism since the post-axial lava and seamount lava erupted in a deep-marine environment and there are no constraints on whether the out-of-sequence lava predate or coincide with the uplift.

We evaluated three different scenarios that could explain the observed evolution of Masirah. The first scenario is one where the presence of trace element-enriched melts as well as the progressive increase in trace element enrichment through time is attributed to the influence of hotspot magmatism (e.g., Meyer et al., 1996). Although plume-fed hotspot magmatism typically results in trace element enriched OIB, as well as E-MORB in regions of hotspot-ridge interaction, their REE patterns are characteristically HREE depleted due to melting in the garnet stability field. The LREE enriched dykes and lava on Masirah lack this HREE depletion, inconsistent with deep melting (Figure 7a). Furthermore, the relatively small volumes of the seamount lavas, and the overall thin nature of the igneous axial crust argue against a hotspot origin or contribution, since hotspots tend to be sites of enhanced melting.

The second scenario is one where low-volume (near) off-axis magmatism is generated by the imperfect focusing of melts toward the ridge-axis. Near-axis MORB preserves a larger diversity of melt compositions compared to MORB that erupted on-axis (e.g., Allan et al., 1989; Niu & Batiza, 1997). In a triangular shaped axial melting zone, the height of the melting column, and therefore the degree of melting, decreases with increasing distance off-axis and as a result melts generated off-axis would preferentially sample enriched fusible pyroxenite components in the mantle. Imperfect focusing of such melts preserves their enriched compositions by avoiding homogenization at the ridge axis and instead results in the addition of enriched melts to the off-axis lithosphere as plutons, dykes and erupted lava. Observations of seamount chains extending off-axis along the East Pacific Rise (EPR) suggest that although seamount chains are generally age-progressive (i.e., ages increase with increasing distance off-axis), volcanic activity may persist for up to 100 km off-axis (Allan et al., 1989; Anderson et al., 2021; Romano et al., 2022). For an assumed half-spreading rate of 20 km/Ma at the Masirah paleoridge (Peters, 2000), this would amount to ∼5 Ma, similar to the inferred age difference between the axial and post-axial lava suites on Masirah. Figures 7c and 7d shows that near-axis seamounts (dark-blue triangles) and seamounts that erupt on oceanic lithosphere up to 5 Ma old (light-blue triangles) have a similar compositional ranges, comparable to MORB. Seamounts that form further off-axis (such as "petit spots," green triangles) in contrast show greater trace element enrichments and OIB-like HREE depletion, likely a result of deeper and lower-degree melting underneath a thicker lithospheric lid.

In the third scenario, a specific plate-tectonic event relating to the break-up of East Gondwana and resulting in a reorganization of plate-motion in the Indian Ocean affected axial and off-axis magmatism on Masirah. This event, recorded in the North and West Somali basins in the Indian Ocean at ∼135–130 Ma (Davis et al., 2016; Gaina et al., 2007, 2015), resulted in a change of motion of the Indian Plate, whereupon north-south orientated seafloor

spreading ceased in the North Somali Basin and slowed down with an increased strike-slip component in the West Somali Basin (Figure 1a; Cochran, 1988; Davis et al., 2016; Gaina et al., 2015; Phethean et al., 2016; Reeves et al., 2016). Due to the supposed origin of Masirah at a ridge near the present-day Somali basins (Gnos & Perrin, 1996), previous studies proposed a link between this tectonic event and the later magmatism at Masirah (Marquer et al., 1998; Meyer et al., 1996; Peters, 2000). Our new age for Masirah suggests that the main phase of crustal accretion potentially coincided with this event as well. As seafloor spreading came to a halt, so would asthenospheric upwelling and melting. The resulting lower degrees of melting are expected to preferentially sample the more fusible, enriched mantle components, while reduced homogenization of these lower volume melts increases the preservation potential of the enriched compositions. Additional off-axis low-degree melting could occur during small amounts of asthenospheric upwelling as a result of the accommodation of transpressive and transtensive plate motions along the rheologically weak extinct MOR. A present-day example of this "dying ridge" model can be found on Macquarie Island, a fragment of oceanic lithosphere that formed at a highly segmented, dying spreading ridge south-west of New Zealand and was uplifted to sea level when the plate boundary became obliquely convergent (Varne et al., 2000). Like Masirah, basalts from Macquarie Island and other parts of the Macquarie ridge are notable for their trace element enrichments (E-MORB and greater enrichments) and distinct isotopic signatures indicating a heterogeneous mantle source (Figures 7c and 7d; Griffin & Varne, 1980; Jiang et al., 2021; Kamenetsky & Maas, 2002; Kamenetsky et al., 2000).

It is difficult to differentiate between the imperfect melt-focusing and dying ridge models for off-axis volcanism. The occurrence of trace element enrichments in both nappes appears to argue against the dying ridge model, since E-MORB and Nb-enriched melts would be expected to be more abundant closer to the former ridge axis (i.e., in the younger nappe). Instead, the continuous process of imperfect melt-focusing can account for the widespread occurrence of E-MORB and Nb-enriched melts in both the Upper and Lower Nappe. We note, however, that most known modern near-axis seamount chains erupt E-MORB as well as D-MORB (Figures 7c and 7d; Anderson et al., 2021; Niu & Batiza, 1997; Sims et al., 2003), whereas at Masirah late melts have exclusively enriched compositions.

The current constraints on the timing of the exhumation of peridotite and dramatic uplift recorded in the Kalban Unit sediments cannot rule out either scenario. Exhumation of the out-of-sequence mantle could have occurred on-axis along a detachment fault, forming an oceanic core complex (OCC). These structures are common at modern slower-spreading ridges although OCC footwalls are not typically observed uplifted to sea-level (e.g., Escartín et al., 2008). If Masirah formed near a transform fault as hypothesized in previous work (Immenhauser, 1996; Peters & Mercolli, 1998), the formation of a transverse ridge may have provided an additional (off-axis) uplift mechanism, however, similar to the uplift to sea-level recorded at Atlantis Bank (Southwest Indian Ridge; Dick et al., 2000) and transform ridges along the Romanche and Vema fracture zones (Mid-Atlantic Rise; Bonatti, 1978; Bonatti et al., 2005). Alternatively, the changes in tectonic plate motion in the young Indian Ocean occurring at the time could be the cause of vertical tectonism along the extinct spreading-ridge. Geophysical surveys of the West Somali Basin have revealed that this event was accompanied by crustal-scale thrust faults, buckling of the ocean lithosphere and the emplacement of off-axis volcanic edifices and plutons (Sauter et al., 2018).

7.4. The Relationship Between D-MORB and E-MORB on Masirah and Present-Day MORs

The observations presented in this study challenge the practice of describing magmatic systems or mid-ocean ridge segments in their entirety as N-MORB, D-MORB, E-MORB, or OIB, and demonstrate that the compositional evolution of a ridge segment may be complex. Crucially, the axial suite on Masirah shows that D-MORB and E-MORB melts can be sourced from the same melting column and form interbedded lava and mutually crosscutting dykes during ocean crustal accretion. Our data suggest that the range in melt compositions was derived from variable degrees of shallow (spinel-field) melting of a heterogeneous source and was preserved during melt transport and crustal processing (Figure 9). This observation was made possible by the on-land exposure of Masirah, which provided an exceptional opportunity to study and sample the different magmatic units in three dimensions at a level of detail that is not possible for in situ oceanic lithosphere.

To test whether the compositional evolution observed on Masirah could be applicable to MORs in general, we examined the compositional variability of MORB within single ridge segments using the compilation of Gale et al. (2013). Figure 10 shows the La_N/Sm_N and Nb/Y compositions of MORB from the 47 ridge segments (out of
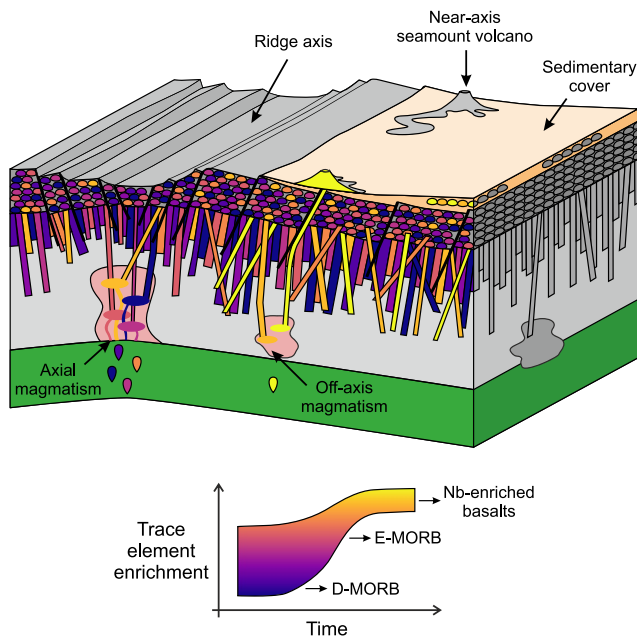
Figure 9. Block diagram illustrating the magmatic evolution of the Masirah dykes and lava (not to scale). Colors of the dykes and lava represent the degree of trace element enrichment, and the schematic graph below shows the change in the range of melt trace element compositions through time. Contemporaneous D-MORB to E-MORB magmatism at the ridge axis is followed by near-axis magmatism consisting of E-MORB to more enriched compositions ("Nb-enriched basalts"). Low melt volumes at the Masirah paleoridge axis result in ephemeral and/or spatially disconnected melt lenses, decreasing the effect of a "crustal filter" (i.e., melt mixing and homogenization).

709) that are more than 500 km away from a plume-fed hotspot and have 10 or more samples with La/Sm analyses. Eleven ridge segments (~23%) have a range that spans D-MORB to E-MORB, indicating that the compositional variation present on Masirah also occurs along some (but not all) modern MOR segments. Furthermore, Nb-enriched compositions (Nb/Y > 0.8, star symbols) are present at four ridge segments (~9%) in the compilation: segment "OH-1" at 35°N (south of Oceanographers Transform Fault, TF; segment MARR93 in Gale et al. (2013)), the segment at 0°N (southeast of Romanche TF; MARR168), the segment at 1°S (southeast of Chain TF; MARR171) and the segment at 49°S (south of Agulhas-Falkland TF; MARR244).

Conditions at the Masirah paleoridge may have been especially suited for the preservation of the large range in magmatic compositions due to the reduced magma supply, as discerned from the relatively thin igneous crust (~2 km; Marquer et al., 1998), as well as the primitive nature of the erupted lava and dykes (Figure 4). Observations from modern MORs show that the variability in trace element and isotope compositions inherited from the mantle source decreases with increasing magma supply and increasing magmatic differentiation (Rubin & Sinton, 2007). Higher volumes of magma and increased residence times in crustal magma chambers function as a so-called "crustal filter" that facilitates the homogenization of compositionally distinct melt batches (e.g., Rubin et al., 2009; Shorttle, 2015; Shorttle et al., 2016; Waters et al., 2011). At a sparsely magmatic ridge, a greater range of melt compositions is expected to be preserved since there is less opportunity for magma mixing to occur. In this respect, it is noteworthy that the coexistence of D-MORB and E-MORB within a ridge segment is more prevalent at the slower-spreading segments (<~40 mm/yr; 10 out of 37 segments, ~27%) than at the faster-spreading segments (>~60 mm/yr; 1 out of 10 segments, ~10%; Figure 10), which are typically more magmatically robust.

Lastly, Masirah preserved a well-constrained system that formed off-axis basalts with enriched compositions. Similar E-MORBs and Nb-enriched basalts are found in plume unrelated oceanic seamounts that occur in a variety of settings ranging from near-axis (e.g., Allan et al., 1989) to far off-axis (e.g., Davis et al., 2002; Hirano et al., 2006). They furthermore appear to have a greater preservation potential during subduction, as illustrated by the accretion of trace element enriched seamounts in Costa Rica (Buchs et al., 2011) and Anglesey, UK (Saito et al., 2015), as well as the widespread occurrence of alkali basalts in the Tethyan realm (e.g., the Haybi volcanics; Searle et al., 1980). Despite differences in tectonic setting, many of these rocks appear similar in terms of formation by low degrees of melting of an enriched mantle source (e.g., Fitton, 2007). Our study shows that such seamounts do not necessarily require a deep mantle source and can instead be formed from the same heterogeneous mantle that underlies the spreading ridge.

8. Conclusions

1. New high-precision U-Pb dating of single zircons indicates that magmatism on Masirah occurred in a shorter time window than previously thought. The oceanic crust was accreted at 135 Ma (Lower Nappe) and 130 Ma (Upper Nappe), refuting earlier models where seafloor spreading took place at approximately 150 Ma and was followed by intraplate magmatism at approximately 130 Ma. Two crosscutting intrusions yielded a ~66 Ma age, coinciding with the proposed Late Cretaceous/Early Paleocene emplacement age of the Eastern Oman Ophiolites.
2. The bulk of the Masirah igneous crust was formed by contemporaneous D-MORB and E-MORB magmatism produced by melting a heterogeneous mantle, while later melts reflect an increasing contribution of low-degree spinel-stability field melting of the enriched component in the source. The significant overlap in trace element compositions of the axial and off-axis dykes and lava units suggests that they formed during a transitional magmatic event where the main phase of crustal accretion was followed by "near-axis" magmatism.
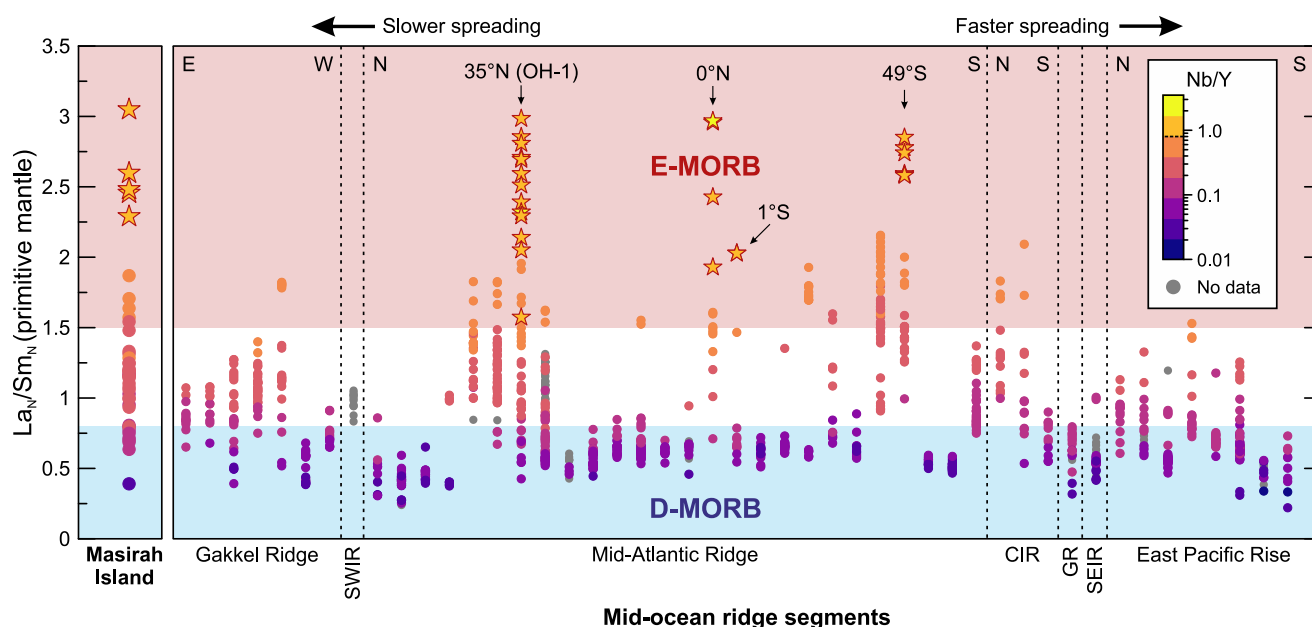
Figure 10. Masirah axial dykes and lava La_N/Sm_N compositions (left) compared to present-day MORB variations within individual MOR spreading segments (from Gale et al. (2013)) showing that the wide compositional variability in Masirah is mirrored in certain parts of the slower spread mid-ocean ridge system. MORB data are filtered to exclude segments within 500 km from a plume-fed hotspot as well as segments that have fewer than 10 samples with La/Sm analyses. Data are normalized to primitive mantle (McDonough & Sun, 1995) and colored by Nb/Y content, with star symbols indicating Nb-enriched compositions (Nb/Y > 0.8). CIR = Central Indian Ridge, GR = Galapagos Ridge, SEIR = Southeast Indian Ridge, SWIR = Southwest Indian Ridge.

3. Trace element compositions of the dykes and lava are inconsistent with a mantle plume origin for the later melts. Instead, they can be produced from the same heterogeneous source that generated the axial melts and show a likeness with (a) near-axis seamounts formed by the imperfect focusing of melts to the ridge axis or (b) basalts erupted at Macquarie Island. The latter represents a dying ridge and the reorganization of plate motions that occurred in the Indian Ocean around ~135–130 Ma possibly contributed to a slow-down and cessation of seafloor spreading at the Masirah paleoridge. Further isotopic and geochronological constraints on the late magmatism are needed to definitively differentiate between these two alternatives.

4. Compilations of MORB show that D- and E-MORB basalts (including Nb-enriched basalts) also occur side by side along the present-day MOR-system, especially at slower ridges. We propose that the contemporaneous D- and E-MORB magmatism observed on Masirah is common along MORs but is only recorded in basalts that erupted at ridge segments with a reduced magma supply and a weaker crustal filter.

Data Availability Statement

The geochemical data presented in this study can be accessed at the EarthChem Library (Jansen et al., 2024a) and the geochronological data can be accessed at the NERC National Geoscience Data Centre (Jansen et al., 2024b). All data are included in Supporting Information S2.

References

Abbotts, I. L. (1978). High-potassium granites in the Masirah ophiolite of Oman. *Geological Magazine*, *115*(6), 415–425. https://doi.org/10.1017/s0016756800041716

Abbotts, I. L. (1979). *A field, petrological and geochemical study of the Masirah ophiolite, Oman*. [Ph.D.]. University of Birmingham.

Albarède, F., Luais, B., Fitton, G., Semet, M., Kaminski, E., Upton, B. G. J., et al. (1997). The geochemical regimes of Piton de la Fournaise Volcano (Réunion) during the last 530 000 years. *Journal of Petrology*, *38*(2), 171–201. https://doi.org/10.1093/petrology/38.2.171

Allan, J. F., Batiza, R., Perfit, M. R., Fornari, D. J., & Sack, R. O. (1989). Petrology of lavas from the Lamont seamount chain and adjacent East Pacific Rise, 10°N. *Journal of Petrology*, *30*(5), 1245–1298. https://doi.org/10.1093/petrology/30.5.1245

Anderson, M., Wanless, V. D., Perfit, M., Conrad, E., Gregg, P., Fornari, D., & Ridley, W. I. (2021). Extreme heterogeneity in mid-ocean ridge mantle revealed in lavas from the 8°20′N near-axis seamount chain. *Geochemistry, Geophysics, Geosystems*, *22*(1), 1–22. https://doi.org/10.1029/2020GC009322

Barton, P. J., Owen, T. R. E., & Wright, R. S. (1990). Preliminary results and interpretation extensional. *Tectonophysics*, *173*(1–4), 319–331. https://doi.org/10.1016/0040-1951(90)90227-y

Batiza, R., & Niu, Y. (1992). Petrology and magma chamber processes at the East Pacific Rise ∼9°30′N. *Journal of Geophysical Research*, *97*(B5), 6779–6797. https://doi.org/10.1029/92JB00172

Beauchamp, W. H., Ries, A. C., Coward, M. P., & Miles, J. A. (1995). Masirah Graben, Oman: A hidden Cretaceous rift basin? *American Association of Petroleum Geologists Bulletin*, *79*(6), 864–879. https://doi.org/10.1306/8d2b1bd8-171e-11d7-8645000102c1865d

Bonatti, E. (1978). Vertical tectonism in oceanic fracture zones. *Earth and Planetary Science Letters*, *37*(3), 369–379. https://doi.org/10.1016/0012-821x(78)90052-3

Bonatti, E., Brunelli, D., Buck, W. R., Cipriani, A., Fabretti, P., Ferrante, V., et al. (2005). Flexural uplift of a lithospheric slab near the Vema transform (Central Atlantic): Timing and mechanisms. *Earth and Planetary Science Letters*, *240*(3), 642–655. https://doi.org/10.1016/j.epsl.2005.10.010

Breton, T., Nauret, F., Pichat, S., Moine, B., Moreira, M., Rose-Koga, E. F., et al. (2013). Geochemical heterogeneities within the Crozet hotspot. *Earth and Planetary Science Letters*, *376*, 126–136. https://doi.org/10.1016/j.epsl.2013.06.020

Buchs, D. M., Arculus, R. J., Baumgartner, P. O., & Ulianov, A. (2011). Oceanic intraplate volcanoes exposed: Example from seamounts accreted in Panama. *Geology*, *39*(4), 335–338. https://doi.org/10.1130/G31703.1

Cannat, M. (1993). Emplacement of mantle rocks in the seafloor. *Journal of Geophysical Research*, *98*(B3), 4163–4172. https://doi.org/10.1029/92jb02221

Cannat, M. (1996). How thick is the magmatic crust at slow spreading oceanic ridges? *Journal of Geophysical Research*, *101*(B2), 2847–2857. https://doi.org/10.1029/95jb03116

Cochran, J. R. (1988). Somali Basin, Chain Ridge, and origin of the Northern Somali Basin gravity and geoid low. *Journal of Geophysical Research*, *93*(B10), 11985–12008. https://doi.org/10.1029/jb093ib10p11985

Cohen, K. M., Finney, S. C., Gibbard, P. L., & Fan, J.-X. (2013). The ICS international chronostratigraphic chart. *Episodes*, *36*(3), 199–204. https://doi.org/10.18814/epiiugs/2013/v36i3/002

Davis, A. S., Clague, D. A., Bohrson, W. A., Dalrymple, G. B., & Greene, H. G. (2002). Seamounts at the continental margin of California: A different kind of oceanic intraplate volcanism. *Bulletin of the Geological Society of America*, *114*(3), 316–333. https://doi.org/10.1130/0016-7606(2002)114<0316:SATCMO>2.0.CO;2

Davis, J. K., Lawver, L. A., Norton, I. O., & Gahagan, L. M. (2016). New Somali Basin magnetic anomalies and a plate model for the early Indian Ocean. *Gondwana Research*, *34*, 16–28. https://doi.org/10.1016/j.gr.2016.02.010

de Graaff, S. J., Goodenough, K. M., Klaver, M., Lissenberg, C. J., Jansen, M. N., Millar, I., & Davies, G. R. (2019). Evidence for a moist to wet source transition throughout the Oman-UAE ophiolite, and implications for the geodynamic history. *Geochemistry, Geophysics, Geosystems*, *20*(2), 651–672. https://doi.org/10.1029/2018GC007923

Dick, H. J. B., Lin, J., & Schouten, H. (2003). An ultraslow-spreading class of ocean ridge. *Nature*, *426*(6965), 405–412. https://doi.org/10.1038/nature02128

Dick, H. J. B., Natland, J. H., Alt, J. C., Bach, W., Bideau, D., Gee, J. S., et al. (2000). A long in situ section of the lower ocean crust: Results of ODP Leg 176 drilling at the Southwest Indian Ridge. *Earth and Planetary Science Letters*, *179*(1), 31–51. https://doi.org/10.1016/S0012-821X(00)00102-3

Donnelly, K. E., Goldstein, S. L., Langmuir, C. H., & Spiegelman, M. (2004). Origin of enriched ocean ridge basalts and implications for mantle dynamics. *Earth and Planetary Science Letters*, *226*(3–4), 347–366. https://doi.org/10.1016/j.epsl.2004.07.019

Doucet, S., Weis, D., Scoates, J. S., Debaille, V., & Giret, A. (2004). Geochemical and Hf-Pb-Sr-Nd isotopic constraints on the origin of the Amsterdam-St. Paul (Indian Ocean) hotspot basalts. *Earth and Planetary Science Letters*, *218*(1–2), 179–195. https://doi.org/10.1016/S0012-821X(03)00636-8

Dumitrica, P., Immenhauser, A., & Dumitrica-Jud, R. (1997). Mesozoic radiolarian biostratigraphy from Masirah ophiolite, Sultanate of Oman— Part 1: Middle Triassic, uppermost Jurassic and lower Cretaceous spumellarians and multisegmented nassellarians. *Bulletin of National Museum of Natural Science*, *9*, 1–106.

Escartín, J., Smith, D. K., Cann, J., Schouten, H., Langmuir, C. H., & Escrig, S. (2008). Central role of detachment faults in accretion of slow-spreading oceanic lithosphere. *Nature*, *455*(7214), 790–794. https://doi.org/10.1038/nature07333

Fitton, J. G. (2007). *The OIB paradox* (Vol. 430, pp. 387–412). Special Paper of the Geological Society of America. https://doi.org/10.1130/2007.2430(20)

Fitton, J. G., Saunders, A. D., Norry, M. J., Hardarson, B. S., & Taylor, R. N. (1997). Thermal and chemical structure of the Iceland plume. *Earth and Planetary Science Letters*, *153*(3–4), 197–208. https://doi.org/10.1016/s0012-821x(97)00170-2

Gaina, C., Müller, R. D., Brown, B., Ishihara, T., & Ivanov, S. (2007). Breakup and early seafloor spreading between India and Antarctica. *Geophysical Journal International*, *170*(1), 151–169. https://doi.org/10.1111/j.1365-246X.2007.03450.x

Gaina, C., Van Hinsbergen, D. J. J., & Spakman, W. (2015). Tectonic interactions between India and Arabia since the Jurassic reconstructed from marine geophysics, ophiolite geology, and seismic tomography. *Tectonics*, *34*(5), 875–906. https://doi.org/10.1002/2014TC003780

Gale, A., Dalton, C. A., Langmuir, C. H., Su, Y., & Schilling, J. G. (2013). The mean composition of ocean ridge basalts. *Geochemistry, Geophysics, Geosystems*, *14*(3), 489–518. https://doi.org/10.1029/2012GC004334

Geshi, N., Umino, S., Kumagai, H., Sinton, J. M., White, S. M., Kisimoto, K., & Hilde, T. W. (2007). Discrete plumbing systems and heterogeneous magma sources of a 24 km^3 off-axis lava field on the western flank of East Pacific Rise, 14°S. *Earth and Planetary Science Letters*, *258*(1–2), 61–72. https://doi.org/10.1016/j.epsl.2007.03.019

Gnos, E., Immenhauser, A., & Peters, T. (1997). Late Cretaceous/early Tertiary convergence between the Indian and Arabian plates recorded in ophiolites and related sediments. *Tectonophysics*, *271*(1–2), 1–19. https://doi.org/10.1016/S0040-1951(96)00249-1

Gnos, E., & Perrin, M. (1996). Formation and evolution of the Masirah ophiolite constrained by paleomagnetic study of volcanic rocks. *Tectonophysics*, *253*(1–2), 53–64. https://doi.org/10.1016/0040-1951(95)00056-9

Gnos, E., & Peters, T. (2003). Mantle xenolith-bearing Maastrichtian to Tertiary alkaline magmatism in Oman. *Geochemistry, Geophysics, Geosystems*, *4*(9), 1–14. https://doi.org/10.1029/2001GC000229

Goodenough, K. M., Thomas, R. J., Styles, M. T., Schofield, D. I., & MacLeod, C. J. (2014). Records of ocean growth and destruction in the Oman–UAE ophiolite. *Elements*, *10*(2), 109–114. https://doi.org/10.2113/gselements.10.2.109

Goričan, Š., O'Dogherty, L., Baumgartner, P. O., Carter, E. S., & Matsuoka, A. (2018). Mesozoic radiolarian biochronology—Current status and future directions. *Revue de Micropaleontologie*, *61*(3–4), 165–189. https://doi.org/10.1016/j.revmic.2018.08.001

Griffin, B. J., & Varne, R. (1980). The Macquarie Island ophiolite complex: Mid-Tertiary oceanic lithosphere from a major ocean basin. *Chemical Geology*, *30*(3), 285–308. https://doi.org/10.1016/0009-2541(80)90109-6

Hall, L. S., Mahoney, J. J., Sinton, J. M., & Duncan, R. A. (2006). Spatial and temporal distribution of a C-like asthenospheric component in the Rano Rahi Seamount Field, East Pacific Rise, 15°-19°S. *Geochemistry, Geophysics, Geosystems*, *7*(3), Q03009. https://doi.org/10.1029/2005GC000994

Hirano, N., Takahashi, E., Yamamoto, J., Abe, N., Ingle, S. P., Kaneoka, I., et al. (2006). Volcanism in response to plate flexure. *Science*, *313*(5792), 1426–1428. https://doi.org/10.1126/science.1128235

Immenhauser, A. (1995). *The autochthonous Mesozoic sediment record on the Masirah Island Ophiolite (Sultanate of Oman)*. [Ph.D.]. Universität Bern.

Immenhauser, A. (1996). Cretaceous sedimentary rocks on the Masirah ophiolite (Sultanate of Oman): Evidence for an unusual bathymetric history. *Journal of the Geological Society*, *153*(4), 539–551. https://doi.org/10.1144/gsjgs.153.4.0539

Immenhauser, A., Schreurs, G., Gnos, E., Oterdoom, H. W., & Hartmann, B. (2000). Late Palaeozoic to Neogene geodynamic evolution of the northeastern Oman margin. *Geological Magazine*, *137*(1), 1–18. https://doi.org/10.1017/S0016756800003526

Immenhauser, A., Schreurs, G., Peters, T., Matter, A., Hauser, M., & Dumitrica, P. (1998). Stratigraphy, sedimentology and depositional environments of the Permian to uppermost Cretaceous Batain Group, eastern-Oman. *Eclogae Geologicae Helvetiae*, *91*(2), 217–235.

Janney, P. E., Macdougall, J. D., Natland, J. H., & Lynch, M. A. (2000). Geochemical evidence from the Pukapuka volcanic ridge system for a shallow enriched mantle domain beneath the South Pacific Superswell. *Earth and Planetary Science Letters*, *181*(1–2), 47–60. https://doi.org/10.1016/S0012-821X(00)00181-3

Jansen, M. N., MacLeod, C. J., Lissenberg, C. J., Parkinson, I. J., & Condon, D. J. (2024a). Whole-rock major and trace element analyses for dykes and lavas of the Masirah ophiolite, SE Oman, version 1.0 [Dataset]. *Interdisciplinary Earth Data Alliance (IEDA)*. https://doi.org/10.60520/IEDA/113125

Jansen, M., MacLeod, C., Lissenberg, J., Parkinson, I., & Condon, D. (2024b). High precision zircon U-Pb data for plutonic rocks from the Masirah and Ra's Madrakah ophiolites, South East Oman [Dataset]. *NERC EDS National Geoscience Data Centre*. https://doi.org/10.5285/3ba7bf8e-0118-4953-86b2-884028d062c4

Jiang, Q., Merle, R. E., Jourdan, F., Olierook, H. K. H., Chiaradia, M., Evans, K. A., et al. (2021). Origin of geochemically heterogeneous mid-ocean ridge basalts from the Macquarie Ridge Complex, SW Pacific. *Lithos*, *380–381*, 105893. https://doi.org/10.1016/j.lithos.2020.105893

Kamenetsky, V. S., Everard, J. L., Crawford, A. J., Varne, R., Eggins, S. M., & Lanyon, R. (2000). Enriched end-member of primitive MORB melts: Petrology and geochemistry of glasses from Macquarie Island (SW Pacific). *Journal of Petrology*, *41*(3), 411–430. https://doi.org/10.1093/petrology/41.3.411

Kamenetsky, V. S., & Maas, R. (2002). Mantle-melt evolution (dynamic source) in the origin of a single MORB suite: A perspective from magnesian glasses of Macquarie Island. *Journal of Petrology*, *43*(10), 1909–1922. https://doi.org/10.1093/petrology/43.10.1909

MacLeod, C. J., Johan Lissenberg, C., & Bibby, L. E. (2013). "Moist MORB" axial magmatism in the Oman ophiolite: The evidence against a mid-ocean ridge origin. *Geology*, *41*(4), 459–462. https://doi.org/10.1130/G33904.1

MacLeod, C. J., & Yaouancq, G. (2000). A fossil melt lens in the Oman ophiolite: Implications for magma chamber processes at fast spreading ridges. *Earth and Planetary Science Letters*, *176*(3–4), 357–373. https://doi.org/10.1016/s0012-821x(00)00020-0

Mahoney, J. J., Frei, R., Tejada, M. L. G., Mo, X. X., Leat, P. T., & Nägler, T. F. (1998). Tracing the Indian Ocean mantle domain through time: Isotopic results from old West Indian, East Tethyan, and South Pacific seafloor. *Journal of Petrology*, *39*(7), 1285–1306. https://doi.org/10.1093/petroj/39.7.1285

Marquer, D., Mercolli, I., & Peters, T. (1998). Early Cretaceous intra-oceanic rifting in the Proto-Indian Ocean recorded in the Masirah ophiolite, Sultanate of Oman. *Tectonophysics*, *292*(1–2), 1–16. https://doi.org/10.1016/S0040-1951(98)00063-8

Marquer, D., Peters, T., & Gnos, E. (1995). A new structural interpretation for the emplacement of the Masirah ophiolites (Oman): A main Paleocene intra-oceanic thrust. *Geodinamica Acta*, *8*(1), 13–19. https://doi.org/10.1080/09853111.1995.11105269

Martinez, M., Aguado, R., Company, M., Sandoval, J., & O'Dogherty, L. (2020). Integrated astrochronology of the Barremian Stage (Early Cretaceous) and its biostratigraphic subdivisions. *Global and Planetary Change*, *195*, 103368. https://doi.org/10.1016/j.gloplacha.2020.103368

Martinez, M., Deconinck, J. F., Pellenard, P., Riquier, L., Company, M., Reboulet, S., & Moiroud, M. (2015). Astrochronology of the Valanginian-Hauterivian stages (Early Cretaceous): Chronological relationships between the Paraná-Etendeka large igneous province and the Weissert and the Faraoni events. *Global and Planetary Change*, *131*, 158–173. https://doi.org/10.1016/j.gloplacha.2015.06.001

Mattinson, J. M. (2005). Zircon U-Pb chemical abrasion ("CA-TIMS") method: Combined annealing and multi-step partial dissolution analysis for improved precision and accuracy of zircon ages. *Chemical Geology*, *220*(1–2), 47–66. https://doi.org/10.1016/j.chemgeo.2005.03.011

McDonough, W. F., & Sun, S.-S. (1995). The composition of the Earth. *Chemical Geology*, *120*(3–4), 223–253. https://doi.org/10.1016/0009-2541(94)00140-4

McLean, N. M., Bowring, J. F., & Bowring, S. A. (2011). An algorithm for U-Pb isotope dilution data reduction and uncertainty propagation. *Geochemistry, Geophysics, Geosystems*, *12*(6), Q0AA18. https://doi.org/10.1029/2010GC003478

Meyer, J., Mercolli, I., & Immenhauser, A. (1996). Off-ridge alkaline magmatism and seamount volcanoes in the Masirah island ophiolite, Oman. *Tectonophysics*, *267*(1–4), 187–208. https://doi.org/10.1016/S0040-1951(96)00094-7

Miyashiro, A. (1973). The Troodos ophiolitic complex was probably formed in an island arc. *Earth and Planetary Science Letters*, *19*(2), 218–224. https://doi.org/10.1016/0012-821x(73)90118-0

Moore, J., White, W. M., Paul, D., Duncan, R. A., Abouchami, W., & Galer, S. J. G. (2011). Evolution of shield-building and rejuvenescent volcanism of Mauritius. *Journal of Volcanology and Geothermal Research*, *207*(1–2), 47–66. https://doi.org/10.1016/j.jvolgeores.2011.07.005

Mountain, G. S., & Prell, W. L. (1990). A multiphase plate tectonic history of the southeast continental margin of Oman. *Geological Society Special Publication*, *49*(49), 725–743. https://doi.org/10.1144/GSL.SP.1992.049.01.44

Nägler, T. F., & Frei, R. (1997). True K-feldspar granites in oceanic crust (Masirah ophiolite, Sultanate of Oman): A U-Pb and Sm-Nd isotope study. *Chemical Geology*, *138*(1–2), 119–126. https://doi.org/10.1016/S0009-2541(96)00155-6

Niu, Y., & Batiza, R. (1997). Trace element evidence from seamounts for recycled oceanic crust in the Eastern Pacific mantle. *Earth and Planetary Science Letters*, *148*(3–4), 471–483. https://doi.org/10.1016/s0012-821x(97)00048-4

Niu, Y., Collerson, K. D., Batiza, R., Wendt, J. I., & Regelous, M. (1999). Origin of enriched-type mid-ocean ridge basalt at ridges far from mantle plumes: The East Pacific Rise at 11°20′N. *Journal of Geophysical Research*, *104*(B4), 7067–7087. https://doi.org/10.1029/1998jb900037

Niu, Y., Regelous, M., Wendt, I. J., Batiza, R., & O'hara, M. J. (2002). Geochemistry of near-EPR seamounts: Importance of source vs. process and the origin of enriched mantle component. *Earth and Planetary Science Letters*, *199*(3–4), 327–345. https://doi.org/10.1016/s0012-821x(02)00591-5

Norris, A., & Danyushevsky, L. (2018). Towards estimating the complete uncertainty budget of quantified results measured by LA-ICP-MS.

O'Neill, H. S. C. (2016). The smoothness and shapes of chondrite-normalized rare earth element patterns in basalts. *Journal of Petrology*, *57*(8), 1463–1508. https://doi.org/10.1093/petrology/egw047

Paul, D., Kamenetsky, V. S., Hofmann, A. W., & Stracke, A. (2007). Compositional diversity among primitive lavas of Mauritius, Indian Ocean: Implications for mantle sources. *Journal of Volcanology and Geothermal Research*, *164*(1–2), 76–94. https://doi.org/10.1016/j.jvolgeores.2007.04.004

Paul, D., White, W. M., & Blichert-Toft, J. (2005). Geochemistry of Mauritius and the origin of rejuvenescent volcanism on oceanic island volcanoes. *Geochemistry, Geophysics, Geosystems*, *6*(6), 1–22. https://doi.org/10.1029/2004gc000883

Pearce, J. A. (1996). Sources and settings of granitic rocks. *Episodes Journal of International Geoscience*, *19*(4), 120–125. https://doi.org/10.18814/epiiugs/1996/v19i4/005

Pearce, J. A., Lippard, S. J., & Roberts, S. (1984). *Characteristics and tectonic significance of supra-subduction zone ophiolites* (Vol. 16, pp. 77–94). Geological Society Special Publication. https://doi.org/10.1144/GSL.SP.1984.016.01.06

Pearce, J. A., & Parkinson, I. J. (1993). *Trace element models for mantle melting: Application to volcanic arc petrogenesis* (Vol. 76, pp. 373–403). Geological Society Special Publication. https://doi.org/10.1144/GSL.SP.1993.076.01.19

Perfit, M. R., Fornari, D. J., Smith, M. C., Bender, J. F., Langmuir, C. H., & Haymon, R. M. (1994). Small-scale spatial and temporal variations in mid-ocean ridge crest magmatic processes. *Geology*, *22*(4), 375–379. https://doi.org/10.1130/0091-7613(1994)022<0375:sssatv>2.3.co;2

Peters, T. (2000). *Formation and evolution of the western Indian Ocean as evidenced by the Masirah ophiolite: A review* (Vol. 349, pp. 525–536). Geological Society of America Special Paper. https://doi.org/10.1130/0-8137-2349-3.525

Peters, T., Immenhauser, A., Mercolli, I., & Meyer, J. (1995). *Geological map of Masirah North and Masirah South with explanatory notes. Sheet K768-North and sheet K768-south, scale 1:50,000* (p. 80). Directorate General of Minerals, Oman Ministry of Petroleum and Minerals.

Peters, T., & Mercolli, I. (1997). Formation and evolution of the Masirah ophiolite (Sultanate of Oman). *Ofioliti*, *22*(1), 15–34.

Peters, T., & Mercolli, I. (1998). Extremely thin oceanic crust in the Proto-Indian Ocean: Evidence from the Masirah ophiolite, Sultanate of Oman. *Journal of Geophysical Research*, *103*(B1), 677–689. https://doi.org/10.1029/97jb02674

Phethean, J. J. J., Kalnins, L. M., van Hunen, J., Biffi, P. G., Davies, R. J., & McCaffrey, K. J. W. (2016). Madagascar's escape from Africa: A high-resolution plate reconstruction for the Western Somali Basin and implications for supercontinent dispersal. *Geochemistry, Geophysics, Geosystems*, *17*(12), 5036–5055. https://doi.org/10.1002/2016gc006624

Prinzhofer, A., Lewin, E., & Allkgre, C. J. (1989). Stochastic melting of the marble cake mantle: Evidence from local study of the East Pacific Rise at 12°50'N. *Earth and Planetary Science Letters*, *92*(2), 189–206. https://doi.org/10.1016/0012-821x(89)90046-0

Reeves, C. V., Teasdale, J. P., & Mahanjane, E. S. (2016). Insight into the eastern margin of Africa from a new tectonic model of the Indian Ocean. *Geological Society Special Publication*, *431*(1), 299–322. https://doi.org/10.1144/SP431.12

Rodriguez, M., Huchon, P., Chamot-Rooke, N., Fournier, M., Delescluse, M., & François, T. (2016). Tracking the paleogene India-Arabia plate boundary. *Marine and Petroleum Geology*, *72*, 336–358. https://doi.org/10.1016/j.marpetgeo.2016.02.019

Rodriguez, M., Huchon, P., Chamot-Rooke, N., Fournier, M., Delescluse, M., Smit, J., et al. (2020). Successive shifts of the India-Africa transform plate boundary during the Late Cretaceous-Paleogene interval: Implications for ophiolite emplacement along transforms. *Journal of Asian Earth Sciences*, *191*, 104225. https://doi.org/10.1016/j.jseaes.2019.104225

Romano, V., Gregg, P. M., Zhan, Y., Fornari, D. J., Perfit, M. R., Wanless, D., et al. (2022). The formation of the 8°20'N seamount chain, East Pacific Rise. *Marine Geophysical Researches*, *43*(4), 42. https://doi.org/10.1007/s11001-022-09502-z

Royer, J. Y., Chaubey, A. K., Dyment, J., Bhattacharya, G. C., Srinivas, K., Yatheesh, V., & Ramprasad, T. (2002). *Paleogene plate tectonic evolution of the Arabian and Eastern Somali basins* (Vol. 195, pp. 7–23). Geological Society Special Publication. https://doi.org/10.1144/GSL.SP.2002.195.01.02

Rubin, K. H., & Sinton, J. M. (2007). Inferences on mid-ocean ridge thermal and magmatic structure from MORB compositions. *Earth and Planetary Science Letters*, *260*(1–2), 257–276. https://doi.org/10.1016/j.epsl.2007.05.035

Rubin, K. H., Sinton, J. M., MacLennan, J., & Hellebrand, E. (2009). Magmatic filtering of mantle compositions at mid-ocean-ridge volcanoes. *Nature Geoscience*, *2*(5), 321–328. https://doi.org/10.1038/ngeo504

Saito, T., Uno, M., Sato, T., Fujisaki, W., Haraguchi, S., Li, Y. B., et al. (2015). Geochemistry of accreted metavolcanic rocks from the Neo-proterozoic Gwna Group of Anglesey-Lleyn, NW Wales, U.K.: MORB and OIB in the Iapetus Ocean. *Tectonophysics*, *662*, 243–255. https://doi.org/10.1016/j.tecto.2015.08.015

Von Salis, K., & Immenhauser, A. (1997). Mesozoic calcareous nannofossils from Masirah Island (Sultanate of Oman). *Journal of Nannoplankton Research*, *19*(2), 95–101. https://doi.org/10.58998/jnr2260

Sauter, D., Cannat, M., Rouméjon, S., Andreani, M., Birot, D., Bronner, A., et al. (2013). Continuous exhumation of mantle-derived rocks at the Southwest Indian Ridge for 11 million years. *Nature Geoscience*, *6*(4), 314–320. https://doi.org/10.1038/ngeo1771

Sauter, D., Ringenbach, J. C., Cannat, M., Maurin, T., Manatschal, G., & McDermott, K. G. (2018). Intraplate deformation of oceanic crust in the West Somali Basin: Insights from long-offset reflection seismic data. *Tectonics*, *37*(2), 588–603. https://doi.org/10.1002/2017TC004700

Schreurs, G., & Immenhauser, A. (1999). West-northwest directed obduction of the Batain Group on the eastern Oman continental margin at the Cretaceous-Tertiary boundary. *Tectonics*, *18*(1), 148–160. https://doi.org/10.1029/1998tc900020

Searle, M. P., Lippard, S. J., Smewing, J. D., & Rex, D. C. (1980). Volcanic rocks beneath the Semail Ophiolite nappe in the northern Oman mountains and their significance in the Mesozoic evolution of Tethys. *Journal of the Geological Society*, *137*(5), 589–604. https://doi.org/10.1144/gsjgs.137.5.0589

Shackleton, R. M., & Ries, A. C. (1990). *Tectonics of the Masirah fault zone and eastern Oman* (Vol. 49, pp. 715–724). Geological Society Special Publication. https://doi.org/10.1144/GSL.SP.1992.049.01.43

Shackleton, R. M., Ries, A. C., Bird, P. R., Filbrandt, J. B., Lee, C. W., & Cunningham, G. C. (1990). *The Batain Melange of NE Oman* (Vol. 49, pp. 673–696). Geological Society Special Publication. https://doi.org/10.1144/GSL.SP.1992.049.01.41

Shorttle, O. (2015). Geochemical variability in MORB controlled by concurrent mixing and crystallisation. *Earth and Planetary Science Letters*, *424*, 1–14. https://doi.org/10.1016/j.epsl.2015.04.035

Shorttle, O., Rudge, J. F., Maclennan, J., & Rubin, K. H. (2016). A statistical description of concurrent mixing and crystallization during MORB differentiation: Implications for trace element enrichment. *Journal of Petrology*, *57*(11–12), 2127–2162. https://doi.org/10.1093/petrology/egw056

Sims, K. W. W., Blichert-Toft, J., Fornari, D. J., Perfit, M. R., Goldstein, S. J., Johnson, P., et al. (2003). Aberrant youth: Chemical and isotopic constraints on the origin of off-axis lavas from the East Pacific Rise, 9°-10°N. *Geochemistry, Geophysics, Geosystems*, *4*(10), 8621. https://doi.org/10.1029/2002GC000443

Smewing, J. D., Abbotts, I. L., Dunne, L. A., & Rex, D. C. (1991). Formation and emplacement ages of the Masirah ophiolite, Sultanate of Oman. *Geology*, *19*(5), 453–456. https://doi.org/10.1130/0091-7613(1991)019<0453:FAEAOT>2.3.CO;2

Sun, S. S., & McDonough, W. F. (1989). Chemical and isotopic systematics of oceanic basalts: Implications for mantle composition and processes. *Geological Society Special Publication*, *42*(1), 313–345. https://doi.org/10.1144/GSL.SP.1989.042.01.19

Varne, R., Brown, A. V., & Falloon, T. (2000). Macquarie Island: Its geology, structural history, and the timing and tectonic setting of its N-MORB to E-MORB magmatism. *Special Paper of the Geological Society of America*, *349*, 301–320. https://doi.org/10.1130/0-8137-2349-3.301

Waters, C. L., Sims, K. W. W., Perfit, M. R., Blichert-Toft, J., & Blusztajn, J. (2011). Perspective on the genesis of E-MORB from chemical and isotopic heterogeneity at 9-10°n East Pacific Rise. *Journal of Petrology*, *52*(3), 565–602. https://doi.org/10.1093/petrology/egq091

Whitmarsh, R. B. (1979). The Owen Basin off the south-east margin of Arabia and the evolution of the Owen Fracture Zone. *Geophysical Journal of the Royal Astronomical Society*, *58*(2), 441–470. https://doi.org/10.1111/j.1365-246X.1979.tb01034.x

Workman, R. K., & Hart, S. R. (2005). Major and trace element composition of the depleted MORB mantle (DMM). *Earth and Planetary Science Letters*, *231*(1), 53–72. https://doi.org/10.1016/j.epsl.2004.12.005

Yang, S., Humayun, M., & Salters, V. J. M. (2020). Elemental constraints on the amount of recycled crust in the generation of mid-oceanic ridge basalts (MORBs). *Science Advances*, *6*(26), 1–12. https://doi.org/10.1126/sciadv.aba2923

Zhang, S. Q., Mahoney, J. J., Mo, X. X., Ghazi, A. M., Milani, L., Crawford, A. J., et al. (2005). Evidence for a widespread Tethyan upper mantle with Indian-Ocean-type isotopic characteristics. *Journal of Petrology*, *46*(4), 829–858. https://doi.org/10.1093/petrology/egi002

References From the Supporting Information

Chen, Y., Niu, Y., Wang, X., Gong, H., Guo, P., Gao, Y., & Shen, F. (2019). Petrogenesis of ODP Hole 735B (Leg 176) oceanic plagiogranite: Partial melting of gabbros or advanced extent of fractional crystallization? *Geochemistry, Geophysics, Geosystems*, *20*(6), 2717–2732. https://doi.org/10.1029/2019GC008320

Condon, D. J., Schoene, B., McLean, N. M., Bowring, S. A., & Parrish, R. R. (2015). Metrology and traceability of U–Pb isotope dilution geochronology (EARTHTIME Tracer Calibration Part I). *Geochimica et Cosmochimica Acta*, *164*, 464–480. https://doi.org/10.1016/j.gca.2015.05.026

Dosso, L., Bougault, H., Beuzart, P., Calvez, J.-Y., & Joron, J.-L. (1988). the geochemical structure of the South-East Indian Ridge. *Earth and Planetary Science Letters*, *88*(1–2), 41–59. https://doi.org/10.1016/0012-821x(88)90045-3

Eggins, S. M. (2003). Laser ablation ICP-MS analysis of geological materials prepared as lithium borate glasses. *Geostandards Newsletter*, *27*(2), 147–162. https://doi.org/10.1111/j.1751-908X.2003.tb00642.x

Hamelin, B., Dupré, B., & Allègre, C. J. (1986). Pb-Sr-Nd isotopic data of Indian Ocean ridges: New evidence of large-scale mapping of mantle heterogeneities. *Earth and Planetary Science Letters*, *76*(3–4), 288–298. https://doi.org/10.1016/0012-821x(86)90080-4

Hiess, J., Condon, D. J., McLean, N., & Noble, S. R. (2012). ^{238}U/^{235}U systematics in terrestrial uranium-bearing minerals. *Science*, *335*(6076), 1610–1614. https://doi.org/10.1126/science.1215507

Jaffey, A. H., Flynn, K. F., Glendenin, L. E., Bentley, W. C., & Essling, A. M. (1971). Precision measurement of half-lives and specific activities of ^{235}U and ^{238}U. *Physical Review C*, *4*(5), 1889–1906. https://doi.org/10.1103/PhysRevC.4.1889

Jochum, K. P., Nohl, U., Herwig, K., Lammel, E., Stoll, B., & Hofmann, A. W. (2005). GeoReM: A new geochemical database for reference materials and isotopic standards. *Geostandards and Geoanalytical Research*, *29*(3), 333–338. https://doi.org/10.1111/j.1751-908X.2005.tb00904.x

Jochum, K. P., Weis, U., Schwager, B., Stoll, B., Wilson, S. A., Haug, G. H., et al. (2016). Reference values following ISO guidelines for frequently requested rock reference materials. *Geostandards and Geoanalytical Research*, *40*(3), 333–350. https://doi.org/10.1111/j.1751-908X.2015.00392.x

Jochum, K. P., Weis, U., Stoll, B., Kuzmin, D., Yang, Q., Raczek, I., et al. (2011). Determination of reference values for NIST SRM 610–617 glasses following ISO guidelines. *Geostandards and Geoanalytical Research*, *35*(4), 397–429. https://doi.org/10.1111/j.1751-908X.2011.00120.x

Keller, C. B., Schoene, B., & Samperton, K. M. (2018). A stochastic sampling approach to zircon eruption age interpretation. *Geochemical Perspectives Letters*, *8*, 31–35. https://doi.org/10.7185/geochemlet.1826

Lehnert, K., Su, Y., Langmuir, C. H., Sarbas, B., & Nohl, U. (2000). A global geochemical database structure for rocks. *Geochemistry, Geophysics, Geosystems*, *1*(5), 1012. https://doi.org/10.1029/1999GC000026

Lissenberg, C. J., Rioux, M., Shimizu, N., Bowring, S. A., & Mével, C. (2009). Zircon dating of oceanic crustal accretion. *Science*, *323*(5917), 1048–1050. https://doi.org/10.1126/science.1167330

Longerich, H. P., Jackson, S. E., & Günther, D. (1996). Inter-laboratory note. Laser ablation inductively coupled plasma mass spectrometric transient signal data acquisition and analyte concentration calculation. *Journal of Analytical Atomic Spectrometry*, *11*(9), 899–904. https://doi.org/10.1039/JA9961100899

Mahoney, J. J., Natland, J. H., White, W. M., Poreda, R., Bloomer, S. H., Fisher, R. L., & Baxter, A. N. (1989). Isotopic and geochemical provinces of the western Indian Ocean spreading centers. *Journal of Geophysical Research*, *94*(B4), 4033–4052. https://doi.org/10.1029/JB094iB04p04033

McLean, N. M., Condon, D. J., Schoene, B., & Bowring, S. A. (2015). Evaluating uncertainties in the calibration of isotopic reference materials and multi-element isotopic tracers (EARTHTIME Tracer Calibration Part II). *Geochimica et Cosmochimica Acta*, *164*, 481–501. https://doi.org/10.1016/j.gca.2015.02.040

Michard, A., Montigny, R., & Schlich, R. (1986). Geochemistry of the mantle beneath the Rodriguez Triple Junction and the South-East Indian Ridge. *Earth and Planetary Science Letters*, *78*(1), 104–114. https://doi.org/10.1016/0012-821x(86)90176-7

Niu, Y., Gilmore, T., Mackie, S., Greig, A., & Bach, W. (2002). Mineral chemistry, whole-rock compositions, and petrogenesis of Leg 176 gabbros: Data and discussion. *Proceedings of the Ocean Drilling Program, Scientific Results*, *176*, 1–60. https://doi.org/10.2973/odp.proc.sr.176.011.2002

Pearce, J. A. (1996). A user's guide to basalt discrimination diagrams. In *Geological association of Canada, short course notes* (Vol. 12, pp. 79–113). Retrieved from https://www.researchgate.net/profile/Julian_Pearce2/publication/238170061_A_User's_Guide_to_Basalt_Discrimination_Diagrams/links/00b7d536a1cd5bede4000000.pdf

Pearce, J. A., & Norry, M. J. (1979). Petrogenetic implications of Ti, Zr, Y, and Nb Variations in volcanic rocks. *Contributions to Mineralogy and Petrology*, *69*(1), 33–47. https://doi.org/10.1007/bf00375192

Peng, Z. X., & Mahoney, J. J. (1995). Drillhole lavas from the northwestern Deccan Traps, and the evolution of Réunion hotspot mantle. *Earth and Planetary Science Letters*, *134*(1–2), 169–185. https://doi.org/10.1016/0012-821x(95)00110-x

Rioux, M., Johan Lissenberg, C., McLean, N. M., Bowring, S. A., MacLeod, C. J., Hellebrand, E., & Shimizu, N. (2012). Protracted timescales of lower crustal growth at the fast-spreading East Pacific Rise. *Nature Geoscience*, *5*(4), 275–278. https://doi.org/10.1038/ngeo1378

Salters, V. J. M., & White, W. M. (1998). Hf isotope constraints on mantle evolution. *Chemical Geology*, *145*(3–4), 447–460. https://doi.org/10.1016/s0009-2541(97)00154-x

Sheth, H. C., Mahoney, J. J., & Baxter, A. N. (2003). Geochemistry of lavas from Mauritius, Indian ocean: Mantle sources and petrogenesis. *International Geology Review*, *45*(9), 780–797. https://doi.org/10.2747/0020-6814.45.9.780

Staudigel, H. (2014). 4.16—Chemical fluxes from hydrothermal alteration of the oceanic crust. In H. D. Holland, & K. K. Turekian (Eds.), *Treatise on geochemistry* (2nd ed., pp. 583–606). Elsevier. https://doi.org/10.1016/B978-0-08-095975-7.00318-1

Vermeesch, P. (2018). IsoplotR: A free and open toolbox for geochronology. *Geoscience Frontiers*, *9*(5), 1479–1493. https://doi.org/10.1016/j.gsf.2018.04.001

Wendt, I., & Carl, C. (1991). The statistical distribution of the mean squared weighted deviation. *Chemical Geology*, *86*(4), 275–285. https://doi.org/10.1016/0168-9622(91)90010-t

White, W. M. (1993). $^{238}U/^{204}Pb$ in MORB and open system evolution of the depleted mantle. *Earth and Planetary Science Letters*, *115*(1–4), 211–226. https://doi.org/10.1016/0012-821x(93)90223-v

Zhang, C., Koepke, J., France, L., & Godard, M. (2017). Felsic plutonic rocks from IODP Hole 1256D, Eastern Pacific: Implications for the nature of the axial melt lens at fast-spreading mid-ocean ridges. *Journal of Petrology*, *58*(8), 1535–1566. https://doi.org/10.1093/petrology/egx064